Cryogenic Testing of an Electromagnetic Actuation System for Low Temperature Slit Masks

By

Paul Francescutti
Bachelor in Engineering, University of Victoria, 2004

A Thesis Submitted in Partial fulfillment of the Requirements for the Degree of

MASTER OF APPLIED SCIENCE
in the
Department of Mechanical Engineering

© Paul Francescutti, 2006
University of Victoria

All rights reserved. This thesis may not be reproduced in whole or in part, by photocopy or other means, without the express written permission of the author.

Cryogenic Testing of an Electromagnetic Actuation System for Low Temperature Slit Masks

By

Paul Francescutti
Bachelor in Engineering, University of Victoria, 2004

Supervisory Committee

Dr. A. Rowe, (Department of Mechanical Engineering)
Supervisor

Dr. B. Buckham, (Department of Mechanical Engineering)
Department Member

Dr. C. Bradley, (Department of Mechanical Engineering)
Department Member

Outside Member

Rudolphe Conan
External Examiner

Supervisory Committee

Dr. A. Rowe, (Department of Mechanical Engineering)
Supervisor

Dr. B. Buckham, (Department of Mechanical Engineering)
Department Member

Dr. C. Bradley, (Department of Mechanical Engineering)
Department Member

Outside Member

Rudolphe Conan
External Examiner

Abstract

The James Web Space telescope will replace the aging Hubble in 2012. One instrument onboard will be the Near Infrared Spectroscope which will require a reconfigurable slit mask to control light incident upon it. One design for this device is called the *Mechanically Actuated Reconfigurable Slit mask* (MARS). The MARS uses several electromagnetic clamps to move shutters though the focal plane. The goal of this thesis is to develop a system to characterise these clamps at cryogenic temperatures. FEA simulations predicted clamp performance and aided in the development of a test apparatus. An apparatus which utilises the Lorentz force to force the clamp jaws open was developed, built and tested. The device was built inside a cryostat which operated at 30 K. It was found that the test apparatus performed as intended. The clamps themselves proved to be problematic. Small perturbations or misalignments caused significant inconsistencies in experimental results.

Table of Contents

SUPERVISORY COMMITTEE ..... **I**

ABSTRACT ..... **II**

TABLE OF CONTENTS ..... **III**

LIST OF FIGURES ..... **VI**

LIST OF TABLES ..... **VIII**

NOMENCLATURE ..... **IX**

ACKNOWLEDGMENTS ..... **X**

CHAPTER 1 INTRODUCTION **1**

1.1 MOTIVATION 1

1.2 MARS DEVICE 3

1.2.1 Actuation Method *6*

1.3 OBJECTIVES 7

CHAPTER 2 MAGNETISM THEORY AND SIMULATIONS **9**

2.1 CLAMPS 9

2.2 MAGNETISM THEORY 10

2.2.1 Magnetic Circuit Calculations *11*

2.2.2 Ferromagnetism *13*

2.2.3 Low Temperature Effects on Ferromagnetic Materials *15*

2.2.4 Maxwell Stress Tensor *16*

2.2.5 Lorentz Force Law *16*

2.3 FINITE ELEMENT CLAMP GEOMETRY SIMULATIONS 18

2.3.1 Problem Setup *18*

2.3.2 Results of Clamp Shape Experiments *20*

2.3.3 Results of Current Tests *21*

2.3.4 Analysis of FEA Results *23*

2.4 SUMMARY 24

CHAPTER 3 TEST APPARATUS COMPONENT MODELING **25**

3.1 CRYOSTAT AND HEAT SHIELDING 25

3.2 PROBLEM DESCRIPTION 27

3.3 LITERATURE REVIEW FORCE MEASUREMENT 28

3.4 FORCE MEASUREMENT METHOD 30

3.5 PROPOSED MEASUREMENT TECHNIQUE 31
3.6 PERMANENT MAGNETS 32
Permanent Magnet Field Strength Simulations *34*
3.6.1 Permanent Magnet Force Simulations *36*
3.7 PERMANENT MAGNET REFINEMENT 38
3.8 SUMMARY 41

CHAPTER 4 TEST APPARATUS DEVELOPMENT 42

4.1 SYSTEM COMPONENTS 42
4.1.1 Field Generator *42*
4.1.2 Force Coil *43*
4.1.3 Adjustable Mount *46*
4.1.4 Force Link *48*
4.1.5 Link Lock *48*
4.1.6 Complete Assembly *52*
4.2 CALIBRATION AND ACCURACY 53
4.2.1 Calibration Method and Results *54*
4.3 TEST PROCEDURE AND INSTRUMENTATION 57
4.3.1 Experimental Procedure *57*
4.3.2 Instrumentation Design *58*
4.4 SUMMARY 61

CHAPTER 5 TESTING AND DESIGN REFINEMENT 62

5.1 INITIAL TEST RESULTS 62
5.2 EFFECTS OF FORCE COIL CURRENT RAMP RATE 63
5.3 RESULT VERIFICATION 64
5.4 EFFECTS OF CLAMP TESTING ASSEMBLY ADJUSTMENTS 66
5.4.1 Clamp Jaw Support Assembly *69*
5.4.2 Second Force Link Redesign *71*
5.5 EFFECTS OF CLAMP CURRENT POLARITY 73
5.6 SUMMARY 75

CHAPTER 6 RESULTS AND DISCUSSION 76

6.1 ADDITION OF STAINLESS STEEL SHUTTER 77
6.2 FURTHER REPEATABILITY TESTS 78
6.3 VALIDATION OF TEST APPARATUS 80
6.4 CLAMP DESIGN ANALYSIS 82

CHAPTER 7 CONCLUSIONS 84

7.1 Final Test Apparatus Design 84
7.2 Clamp Design Analysis 85
7.3 Recommendations 86

REFERENCES 87

APPENDIX B - HELMHOLTZ COIL PAIR 90

B.1 Magnetic Field Generated in a Helmholtz Coil 90
B.2 Coil Windings 91
B.3 Heat Generation in the Coils 94
B.4 FEA Field Strength Simulations 94
B.5 Force Simulations 95

List of Figures

FIGURE 1-1: PROPOSED APPLICATION OF A SLIT MASK 1
FIGURE 1-2: SCHEMATIC OF THE PROPOSED SLIT MASK DESIGN AND ITS KEY COMPONENTS 3
FIGURE 1-3: MARS DEVICE EDGE AND ISOMETRIC VIEWS WITH CLAMPS AND ACTUATORS REMOVED [2] 4
FIGURE 1-4: MARS FOCAL PLANE [2] 5
FIGURE 1-5: MARS DEVICE, WITH ACTUATORS AND CLAMPS [2] 5
FIGURE 1-6: INDIVIDUAL STEPS OF SHUTTER DISPLACEMENT 7
FIGURE 2-1: ORIGINAL CLAMP DESIGN 9
FIGURE 2-2: SIMPLIFIED MAGNETIC CIRCUIT 11
FIGURE 2-3: TYPICAL HYSTERESIS LOOPS FOR A FERROMAGNETIC MATERIAL [3] 14
FIGURE 2-4: B-H CURVES FOR HYMU 80 AND HIGH-PERM 49 [4] 14
FIGURE 2-5: SATURATION MAGNETIZATION VS. TEMPERATURE [3] 15
FIGURE 2-6: CROSS SECTION OF CLAMP SHOWING COIL CURRENTS 19
FIGURE 2-7: FEA MODEL SHOWING THE CLAMP BAR AND THE COIL REGIONS 19
FIGURE 2-8: RESULTS OF FORCE CALCULATIONS FOR HIGH-PERM 49 AND HYMU 80 21
FIGURE 2-9: CLAMPING FORCE AND CORE FLUX DENSITY VERSUS COIL CURRENT FOR HYMU 80 AND HIGH-PERM 49 (GEOMETRY #19) 22
FIGURE 2-10: CLAMPING FORCE AND CORE FLUX DENSITY VS. COIL CURRENT FOR BOTH MODEL #1 AND #19 22
FIGURE 3-1: CRYOGENIC CHAMBER TO BE USED FOR TESTING 28
FIGURE 3-2: MIYAGI UNIVERSITY TEST APPARATUS DIAGRAM [8] 29
FIGURE 3-3: GENERAL ACTUATOR COMPONENTS 32
FIGURE 3-4: TWO OPTIONS FOR FIELD GENERATOR DESIGN 32
FIGURE 3-5: TWO POSSIBLE PERMANENT MAGNET CONFIGURATIONS, A) TOP STACKED B) BOTTOM STACKED 33
FIGURE 3-6: FEA MODELS OF BOTTOM AND TOP STACKED PERMANENT MAGNET FIELD GENERATORS 34
FIGURE 3-7: FLUX DENSITY, B, THROUGH THE GAP OF A ONE MAGNET FIELD GENERATOR 34
FIGURE 3-8: PEEK FLUX VERSES NUMBER OF MAGNETS FOR BOTH THE TOP AND BOTTOM STACKED FIELD GENERATORS 35
FIGURE 3-9: ERROR BETWEEN F AND F_0 FOR FORCE COIL CURRENT DENSITY FROM ZERO TO MAXIMUM 37
FIGURE 3-10: PERMANENT MAGNETS ARRANGED TO PRODUCE MAXIMUM FIELD THROUGH THE FORCE COIL 39
FIGURE 3-11: FLUX DENSITY THROUGH FIELD GENERATOR 39
FIGURE 3-12: RELATIVE PERMEABILITIES OF SEVERAL STEELS AND OTHER MAGNETIC MATERIALS [6] 40
FIGURE 4-1: FINAL FIELD GENERATOR DESIGN 42
FIGURE 4-2: MAGNETIC FORCES ON CURRENT CARRYING COILS IMMERSED IN A MAGNETIC FIELD 44
FIGURE 4-3: FINAL FORCE COIL DESIGN AND ITS POSITION IN THE FIELD GENERATOR 44

FIGURE 4-4: COMPLETE MOUNTING SYSTEM WITH FIELD GENERATOR 47
FIGURE 4-5: TWO PORTIONS OF THE ADJUSTABLE MOUNT 48
FIGURE 4-6: FIRST DESIGN ITERATION OF THE *LINK LOCK* MECHANISM 49
FIGURE 4-7: SECOND DESIGN ITERATION OF THE LINK LOCK MECHANISM 50
FIGURE 4-8: FINAL DESIGN OF THE LINK LOCK MECHANISM 51
FIGURE 4-9: COMPLETE APPARATUS IN CRYOSTAT 52
FIGURE 4-10: CALIBRATION APPARATUS 53
FIGURE 4-11: FORCE COIL ALIGNMENT INSIDE THE FIELD GENERATOR 54
FIGURE 4-12: FORCE VS. OFFSET FROM BASE POINT 55
FIGURE 4-13: FLUX DENSITY IN FIELD GENERATOR ALONG Z-AXIS 55
FIGURE 4-14: FORCE VS. COIL CURRENT GAINED FROM AVERAGE OF SEVERAL CALIBRATION RUNS 56
FIGURE 4-15: SIMPLIFIED CIRCUIT DIAGRAM OF CLAMP OPEN TEST 59
FIGURE 4-16: FRONT PANEL OF DAQ PROGRAM 60
FIGURE 5-1: INITIAL RESULTS 62
FIGURE 5-2: RESULTS OF FORCE COIL CURRENT RAMP RATE EXPERIMENTS 63
FIGURE 5-3: RESULTS OF VERIFICATION EXPERIMENTS 65
FIGURE 5-4: COMPARISON BETWEEN VERIFICATION CURVE AND EXPERIMENTAL RESULTS 66
FIGURE 5-5: RESULTS OF INITIAL CLAMP REPEATABILITY EXPERIMENTS 67
FIGURE 5-6: MASS VERIFICATION OF CLAMP PERFORMANCE AFTER REASSEMBLY 67
FIGURE 5-7: RESULTS OF NEW WIRE-BASED FORCE LINK DESIGN 68
FIGURE 5-8: INITIAL CLAMP DESIGN ASSEMBLY 69
FIGURE 5-9: FINAL CLAMP JAW SUPPORT ASSEMBLY 70
FIGURE 5-10: RESULTS OF NEW CLAMP SUPPORT ASSEMBLY 71
FIGURE 5-11 THREE CONFIGURATIONS OF THE FORCE LINK 72
FIGURE 5-12: RESULTS AFTER THIRD FORCE LINK WAS INSTALLED 73
FIGURE 5-13: FINAL TEST CONFIGURATION RESULTS SHOWING TWO GROUPS OF PERFORMANCE CURVES 74
FIGURE 6-1: INITIAL RESULTS OF CLAMP TESTS WHEN SHUTTER MATERIAL IS ADDED 78
FIGURE 6-2: RESULTS OF REPEATABILITY EXPERIMENTS WITH SHUTTER MATERIAL INSTALLED 79
FIGURE 6-3: RESULTS OF CLAMP JAW REPLACEMENT EXPERIMENTS 80
FIGURE B-0-1: ISOMETRIC AND SECTION VIEW OF A HELMHOLTZ COIL PAIR WITH A RADIUS AND SPACING OF 60MM 90

List of Tables

TABLE 1-1: PERFORMANCE REQUIREMENTS FOR THE MARS DEVICE [1] 2
TABLE 3-1: WARM-UP EXPERIMENT RESULTS 27
TABLE 4-1: COIL DATA FOR COILS CONSTRUCTED FROM EACH WIRE GAUGE 45
TABLE 4-2: DATA ACQUISITION CHANNELS 58
TABLE B-1: PROPERTIES OF STANDARD COPPER WIRE [IEEE STANDARD 835] 92
TABLE B-2: MAGNITUDE OF THE MAGNETIC FLUX DENSITY AT CENTER OF THE HELMHOLTZ COIL PAIR 95

Nomenclature

MARS	-	Acronym, Mechanically Actuated Reconfigurable Slit mask
NIRSpec	-	Acronym, Near Infrared Spectrograph
CCD	-	Acronym, Charge Couple Device
Fill Factor	-	Percent of the total focal plane area in which a slit can be formed
NASA	-	Acronym, National Aeronautics and Space Administration
JWST	-	Acronym, James Web Space Telescope, formerly known as the Next Generation Space Telescope, or NGST
NdFeB	-	Neodymium-Iron-Boron ceramic rare-earth magnets
MLI	-	Acronym, Multi Layer Insulation, also known as super insulation
DAQ	-	Acronym, Data Acquisition

Symbols

A	Area
A_c	Circular area
A_{coil}	Coil cross sectional area
B	Magnetic Flux Density
Br	Remanent flux density
d	Wire diameter
E	Electric field
F	Force
F_{mm}	Magnetomotive force
g	Gravity = 9.81m/s^2
H	Magnetic Field
i	Current
I_{cc}	Clamp Coil Current
I_{fc}	Force coil current
I_{hhc}	Helmholtz coil current
I_w	Wire current
J	Current density
k	Current carrying capacity
l	length
M	Magnetization
m	Mass
M_r	Remanent magnetization
n	number of turns
P	Power
R	Resistance
R_l	Reluctance
R_{total}	Total reluctance
T_c	Currie temperature
v	velocity
μ	Magnetic permeability
μ_0	Permeability of free space = $4\pi x10^{-7}$
μ_r	Relative permeability
Φ	Magnetic flux

Acknowledgments

I would firstly like to acknowledge the aid and support of my supervisor Dr. Andrew Rowe whose assistance, knowledge and personal attention helped make this project possible. I would also like to thank the National Research Council and the National Science and Engineering Research Council of Canada for their financial support as well as Darren Erickson of the NRC Herzberg Institute of Astrophysics for entrusting this project to me and for his professional assistance. A very special thank you to all the students and staff in the UVic engineering Cryo fuels laboratory, my family and friends. Without their constant assistance and support I would not have been able to reach my goals.

Chapter 1 Introduction

1.1 Motivation

Slit masks are opaque screen placed in front of detectors to obscure light from undesired sources. Slits cut into the screen allow light from desired sources to pass through and reach the detector behind it. The function of a slit mask is to control light transmitted onto a detector from one or several sources and are used in several detector applications around the world.. In telescope applications, slit masks are used to obscure light from background stellar objects while allowing light from desired targets to reach detectors behind the slit mask. The simplest slit masks are custom cut from opaque material and placed in front of the detector before each experiment is performed. The development of the James Web Space Telescope has produced the need for a robust, small and effective design for a remotely reconfigurable slit mask. Figure 1-1 shows a simple schematic of a slit mask in a telescope. The light from the target star is allowed to pass through an aperture while the other stars are obscured by the slit mask.

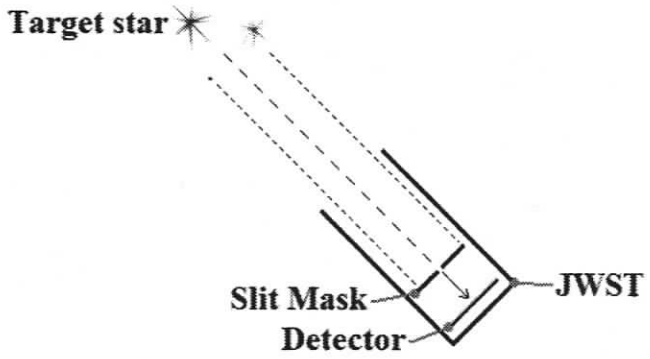

Figure 1-1: Proposed application of a slit mask

The detector for which the slit mask is to be developed is a Near Infrared Spectrograph (*NIRSpec*) These devices are typically isolated from their surroundings in a high vacuum environment and have an operating temperature in the cryogenic regime. This isolation makes installing custom cut slit masks time consuming and difficult even in ground based telescope applications. This problem is compounded in orbital telescopes applications by

the impossibility of manual mask replacement. A remotely reconfigurable slit mask would allow for the placement of a new slit configuration without long warm-up and cool-down delays. To fill the need, engineers at the National Research Council, Herzberg Institute for Astrophysics developed a mechanically actuated reconfigurable slit mask called *MARS*. The MARS device requires significant design refinement in order to improve its performance and reliability. Some of the important design criteria are: low power consumption, small size and mass and fast actuation time. A unique feature of the MARS device is its use of a number of magnetic clamps to grasp and locate the openings in the mask. Before optimizing their design, a means of characterizing their performance is required with clamping force being a primary parameter. This thesis describes the development, testing and optimisation of a test apparatus used to measure clamping forces.

The MARS project was developed to conform to specifications put forward by the European Space Agency (*ESA*). These specifications are outlined in Table 1-1. A more complete list of the design requirements is available in [1].

Table 1-1: Performance requirements for the MARS device [1]

Performance:	Slit width:	Adjustable between 50 μm and 2 mm
	Slit width accuracy:	± 5 % of slit width
	Slit positioning:	± 25 μm from fixed reference
	Fill factor:	>90%
	ON/OFF Contrast:	>2000, with a goal of 10000
	Reconfiguration time:	< 15 min.
Lifetime:	Design Lifetime:	10 Years
	Reconfiguration Cycles:	>50000
	Failures:	No single point, at least 80% working at end of life
Design:	Mass:	<10kg
	Envelope:	600 x 350 x 200 mm
	Heat dissipation:	<100mW during motion, 0 mW while observing

Of these specifications, the most relevant to this thesis *are fill factor* and *heat dissipation*. Fill factor describes the percentage of the focal plane which would not be obscured by the

slit mask mechanism. This specification dictates the amount of sky in the focal plane in which an unobscured slit can be formed.

1.2 MARS Device

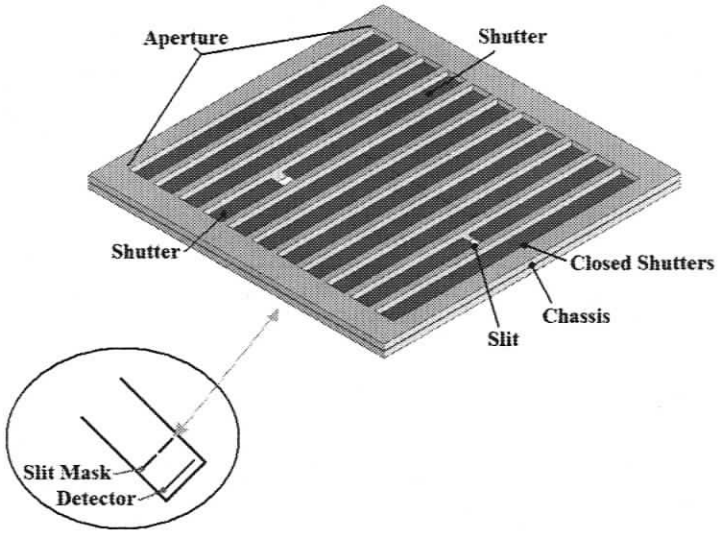

Figure 1-2: Schematic of the proposed slit mask design and its key components

The MARS is made up of an array of apertures in a support chassis. Each aperture represents the area in the focal plain where a slit can be formed. Flexible, opaque shutters are displaced across these apertures in order to create and position slits which allow light to pass through to a NIRSpec closed couple device (*CCD*) positioned behind the slit mask. A simplified representation of the MARS slits and apertures is shown in Figure 1-2. The figure shows how two shutters are used to form each slit. The proposed MARS design features fifty such apertures measuring 4.25mm x 54mm arranged in two columns of twenty five [2]. Two shutters are required for each aperture with one shutter entering from either side. By controlling the position of these two shutters within the aperture, a slit of any width can be placed at any point along the aperture length. If the leading edges of the two shutters are brought together, the aperture can be closed completely.

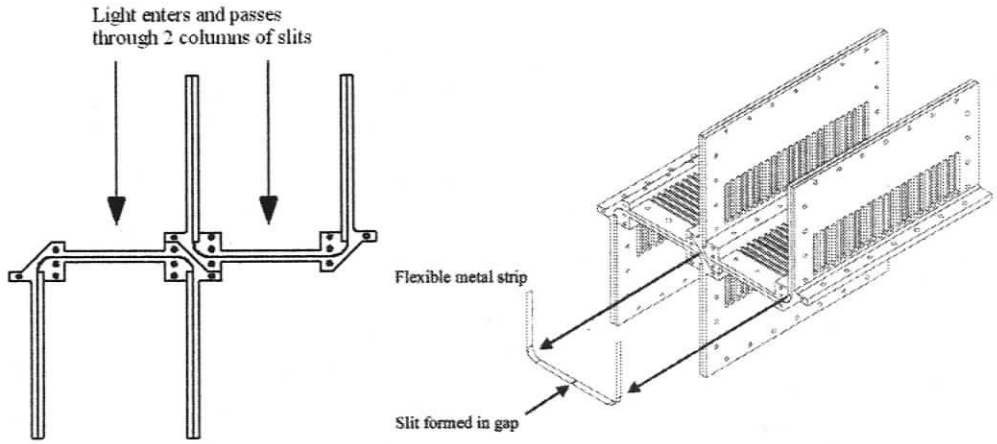

Figure 1-3: MARS device edge and isometric views with clamps and actuators removed [2]

The motion of the shutters is achieved using small electromagnetic clamps in conjunction with piezoelectric actuators. With the apertures arranged in two adjacent columns, it is necessary to include actuators and clamps in the middle of the focal plane. This requirement results in a large portion of the focal plain being obscured by the actuating mechanisms. A large obstruction of the focal plain would reduce the fill factor significantly. The original design of the MARS has a fill factor of 62% which can be increased to 80% if only one column of 25 apertures is used [2]. This does not meet the minimum specifications put forward in Table 1-1 and is one of the motivations for the refinement of the clamps since reducing the clamp size would increase the fill factor. Figure 1-3 shows an edge view of the MARS device with all actuators and clamps removed. The figure illustrates how the device is divided into two halves, identical but inversed. Also in the figure is an isometric view which shows how the shutters are oriented in the MARS device. The shutters make a 90° turn during movement so that the actuating mechanism, located on the vertical portion of the chassis, is oriented perpendicular to the focal plane and the slit apertures. This is intended to minimise the negative impact that the actuating mechanism has on the fill factor.

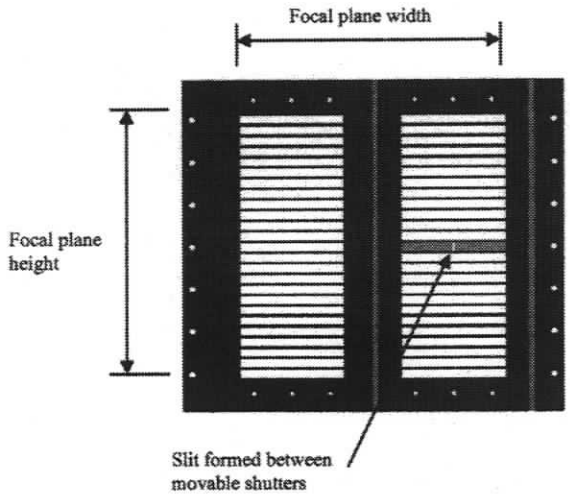

Figure 1-4: MARS focal plane [2]

The determination of the fill factor is shown in Figure 1-4. The fill factor is defined as the combined area of all fifty apertures divided by the total area of the focal plane. The figure shows how the guide bars and the central actuating mechanism structure obscures a large percentage of the focal plane. The central structure is more clearly shown in Figure 1-5. The figure is similar to the second figure in Figure 1-3 but shows a more complete MARS device assembly. Most of the clamps have been removed for clarity and the two remaining clamps are indicated. Reducing the size of the actuators, and thus the amount of obscured focal plain, is the main motivation for the refinement of the electromagnetic clamps.

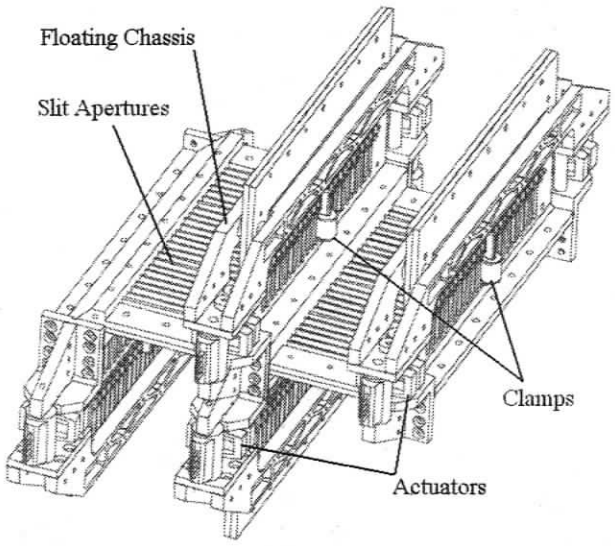

Figure 1-5: MARS device, with actuators and clamps [2]

The clamps represent a significant portion of the cross-sectional area of the actuating mechanism. Therefore, any reduction in the clamp's size would improve the fill factor of the MARS significantly. Other desirable properties for the clamps are low heat dissipation, low mass, and a maximum clamping force for a given coil current. Maximising the clamping force delivered by a given coil current would aid in the reduction of the heat dissipation by reducing the needed current. One of the unspecified parameters is the required clamping force which impacts the entire feasibility of the design. This parameter will need to be determined through characterization of the clamps and tests performed on the MARS prototype. All of these properties will need to be considered during optimisation.

1.2.1 Actuation Method

The motion of the shutters is achieved using the electromagnetic clamps in conjunction with piezoelectric actuators. Each shutter is controlled by a clamp which is energized to grasp its respective shutter. The clamp, along with the secured shutter, is displaced by the actuators. Each aperture requires two clamps, each controlling one shutter. This dictates that the MARS in its original configuration will require one hundred clamps. It would be impractical to have an individual actuator for each clamp because of complexity, space and heat dissipation issues. Instead, all clamps on one end of a column of apertures are to be attached to a floating chassis which is actuated at each end by a pair of piezoelectric actuators. During operation the bar oscillates, moving all the clamps mounted to it. Shutters which are controlled by those clamps can be moved in either direction by controlling when each clamp opens and closes during its oscillation. In this way the shutters will be moved across in discrete steps which will be dictated by the amplitude of the actuator chassis' oscillation. It is proposed that the shutters would be moved over large displacements first with the actuators oscillating at their maximum. Once this bulk displacement is completed, the amplitude of the piezo displacement will be reduced and the fine adjustment of the shutter positions can be performed. Testing will be needed to ensure that the MARS can be reconfigured within the specified time limit stated in Table 1-1. Redundancy will be built into the actuation system to ensure proper operation should an actuator fail.

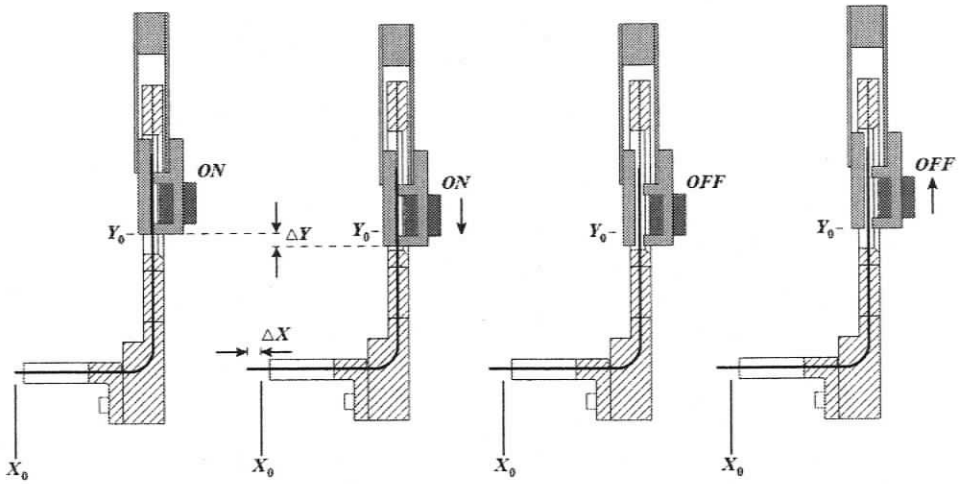

Figure 1-6: Individual steps of shutter displacement

Figure 1-6 shows the individual actions which make up the displacement of the shutters. The initial step involves the activation of the clap which firmly grasps the shutter (shown as a heavy black line). The second step is the displacement of the clamp and shutter by the distance of ΔY which corresponds to the shutter leading edge being displaced by ΔX. The third and four steps involve releasing the shutter and retracing the clamp to its initial position.

1.3 Objectives

The primary objective of the research described in this thesis is to determine the relationship between clamping force and clamp coil current, temperature and clamp material. This objective will include the following goals:

- The development of a cryostat capable of simulating the temperature and pressure conditions that the MARS device will experience in operation.
- The development and testing of a method of applying a controlled force to the clamp jaws.
- Characterise the performance of the prototype clamps.

The following sections are divided into six chapters. Chapter 2 covers all relevant background information and theory. Chapter 3 covers computer modeling of proposed designs as well as a brief literature review of cryogenic force measurement. Chapter four

describes the development of key system components. Chapter five covers the preliminary results and their impact on the design refinement. Chapter six includes experimental results and discussion. Finally, chapter 7 contains conclusions and recommendations for the MARS clamp test assembly project. The two appendices include information on clamp simulations which pertains to section 2.3 and a study of a Helmholtz coil pair based field generator which pertains to section 3.6.

Chapter 2 Magnetism Theory and Simulations

2.1 Clamps

The original clamp design developed at HIA consists of a two piece clamp energized by a single coil. Figure 2-1 shows these three components as they are to be assembled. The coil is wound around the central portion of an F-shaped upper jaw manufactured from high permeability ferromagnetic material and consists of 420 turns. The second component of the clamp is a flat lower jaw which connects the two legs of the F-bar and completes the magnetic circuit. The prototype used 0.05 mm thick stainless-steel shim-stock for shutter material. The gap between the upper and lower jaws corresponds to the thickness of the shutter material which will be positioned between them. The trailing ends of each bar are used to mount them to a flexible support structure. This structure is designed to allow the clamps freedom to move a small distance while maintaining proper alignment.

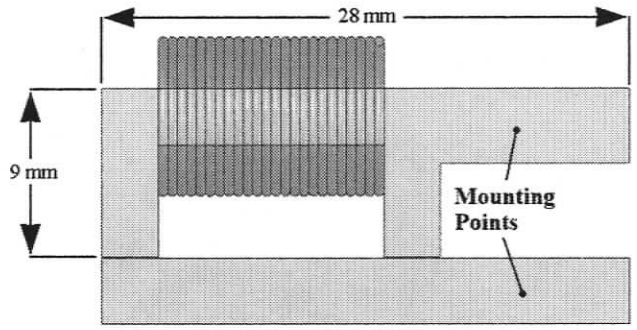

Figure 2-1: Original clamp design

The coil consists of 420 turns of 30AWG copper wire and has an outer diameter of 8-9 mm. The clamp coil current, I_{CC} specified in the original design is 50mA. At room temperature, the clamp coil has a resistance of 2.6 Ω. Using these values, the room temperature heat production can be calculated as follows.

$$P = I_{CC}^2 R = (0.05)^2 \times 2.6 = 6.5mW \tag{2.1}$$

With each clamp producing 6.5 mW of heat, one hundred clamps operating simultaneously would produce 650 mW which is much higher than the limit of 100 mW imposed by the design specifications. However, the resistance of copper is greatly reduced at low temperatures. At 30 K the resistance of the wire is expected to be 3% of its room temperature value [3]. Also, the clamps do not operate continuously during slit reconfiguration. During shutter movement each clamp will have a duty cycle of approximately 50% as it is cycled on and off. Using this information, a new heat production value can be calculated.

$$P = I^2 R = (0.050)^2 \times (0.03 \times 2.6) \times 50\% = 97.5 \mu W \tag{2.2}$$

This calculation shows that if all shutters are being displaced simultaneously, the power dissipated by all 100 clamp coils will be 9.75 mW. This is significantly lower than the specified limit. It also shows that additional apertures and clamps can be added without exceeding the heat production limit.

2.2 Magnetism Theory

Although a magnet's clamping force can be increased by improved its coil current, there is a limit to the amount of magnetization that can be achieved. This limit is dictated by the material from which the clamp is manufactured. The magnetic permeability μ of a magnetic material dictates the relation between the applied magnetic field H and the magnetic flux density B. As pertaining to current carrying coils, H is related to both the current in the coil wire and the number of turns used when making the coil. B is an important property which will later be used to calculate the magnetic force present between the clamping surfaces. These two properties are related by the following equation.

$$B = \mu H \tag{2.3}$$

The relative permeability μ_r is the ratio of the material's permeability to that of free space μ_0 which is defined as the permeability of a complete vacuum and is equal to a constant value of $4\pi \times 10^{-7}\ Wb/Am$; Thus,

$$\mu_r = \frac{\mu}{\mu_0} \tag{2.4}$$

Combining equations (2.3) and (2.4) leads to the following equation for the flux density in the clamp.

$$B = \mu_r \mu_0 H \tag{2.5}$$

The relative permeability of air and several other nonmagnetic materials such as the stainless steel used for the shutters are nearly equal to one. This means that the permeability of these materials is equal to that of free space. The magnetic properties of various materials are commonly described using a plot of B versus H. These plots show the increase in flux density as additional magnetic field is applied. They also show the point of magnetic saturation after which additional applied field does not result in a significant increase in flux density.

2.2.1 Magnetic Circuit Calculations

When calculating the total flux in a magnetic circuit analytically, it is convenient and necessary to simplify the problem. A common method of simplifying magnetic circuits is to define a path in the circuit which approximates the "flow" of the magnetic flux. Figure 2-2 shows such a simplified circuit.

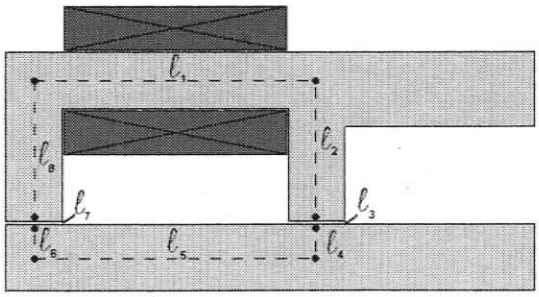

Figure 2-2: Simplified magnetic circuit

The dashed line represents the simplified path of the magnetic field. The points at the nodes divide the path into eight sections. In order to calculate the flux density in the circuit and thus the gaps, the total reluctance R_{total} of the circuit must be found. The total reluctance will be the sum of the reluctances from each of the eight sections. Reluctance is given by equation (2.6), where A is the cross-sectional area and l_i is the length for that section.

$$\mathrm{R_i} = \frac{\ell_i}{\mu_r \mu_o A_i} \tag{2.6}$$

The total flux Φ is given by equation (2.7). The term F_{mm} is known as the magnetomotive force and analogous to the applied field. Magnetomotive force is given by multiplying the wire current by the number of turns in the coil.

$$\Phi = \frac{F_{mm}}{R_{total}} \tag{2.7}$$

The flux density at any point along the path is found by dividing the total flux by the cross-sectional area of the clamp at that point, as shown in equation (2.8).

$$B = \frac{\Phi}{A} \tag{2.8}$$

If equation (2.6) is applied to the MARS clamp, it can be seen that the gap provides the bulk of the total reluctance. For example, compare the reluctance of one gap to that of the longest section in the path, l_1. The length of section l_1 is 15mm which is 300 times longer than the length of the gap which is 0.05mm. The relative permeability of the gap is 1.0 while for the core material varies up to a maximum of ~200000. Applying equation (2.6):

$$R_{gap} = \frac{\ell_{gap}}{1 \times \mu_o A} = \left(\frac{\ell_{gap}}{\mu_o A} \right)$$
$$R_i = \frac{300 \times \ell_{gap}}{\mu_r \mu_o A} = \frac{300}{\mu_r} \left(\frac{\ell_{gap}}{\mu_o A} \right) = \frac{300}{\mu_r} R_{gap} \quad (2.9)$$

The cross-sectional areas for each section are approximately equal so equation (2.8) is valid at any point along the path. From equation (2.9), it can be seen that the reluctance of section l_1 is $300/\mu_r$ times the reluctance of the gap. With the material's μ_r ranging up to 200000, the gap reluctance can be as much as 700 times larger than that for the core. If all the other sectional lengths of the clamps are added together, both gaps are taken into account and all reluctances are summed, the reluctance of the gaps can be as much as 400 times the reluctance of the clamp material. Therefore, reducing the reluctance of the gaps would have a significant effect on the total flux through the circuit. This reduction can be achieved by either reducing the gap width or by increasing the area A of the gap. Because the gap width is dictated by the thickness of the shutters, increasing the area of the gap is the only viable method of reducing its reluctance.

2.2.2 Ferromagnetism

Ferromagnetic materials are characterized by large field dependent permeabilities and commonly exhibit large residual magnetization when field is removed. This residual magnetization is commonly referred to as *remanence* M_r. The *remanent flux density* B_r is simply equal to $\mu_0 M_r$. The characteristics of a ferromagnetic material are best described by its hysteresis loop. The hysteresis loop describes the relation between the magnetization of a material versus the applied field. Another form of the hysteresis loop describes the flux density versus the applied field and is more common. Both forms are shown in Figure 2-3. The four paths which make up a hysteresis loop can be described as magnetization, demagnetization, reverse magnetization and reverse demagnetization. The magnetization shows the flux density as a magnetic field is applied to the material. This curve reaches a saturation point where relation between applied field and flux density becomes linear with slope equal to μ_0. The demagnetization curve shows the flux density as the field is removed. The point where this line crosses the zero-field line is the

remanent flux density. The reverse magnetization and demagnetization curves describe the same properties with an inverted applied field. The dashed lines in Figure 2-3 show the hysteresis loops of a material starting from an unmagnetized state [3].

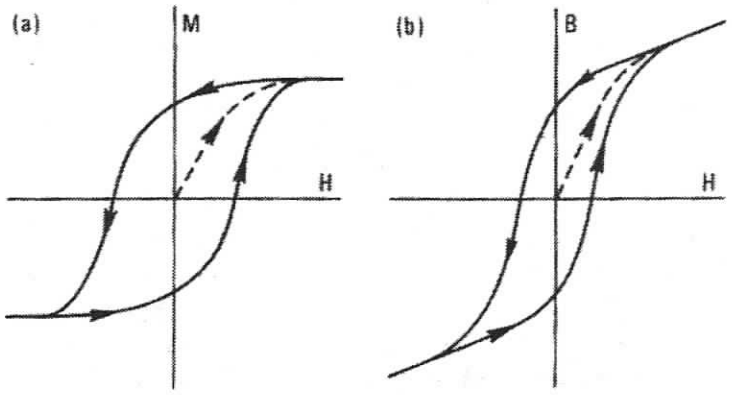

Figure 2-3: Typical hysteresis loops for a ferromagnetic material [3]

The materials used for the manufacture of the MARS clamps are alloys made up primarily of nickel and iron. These alloys, known by their trademark names Hymu 80 and High Perm 49, have a variable μ_r but have little to no remanent flux density. This property is important for the MARS clamps as it will ensure that the clamps fully release with the removal of magnetic field. In such cases, the hysteresis loop disappears and the material behaviour can be shown as a single curve. These curves are shown in Figure 2-4.

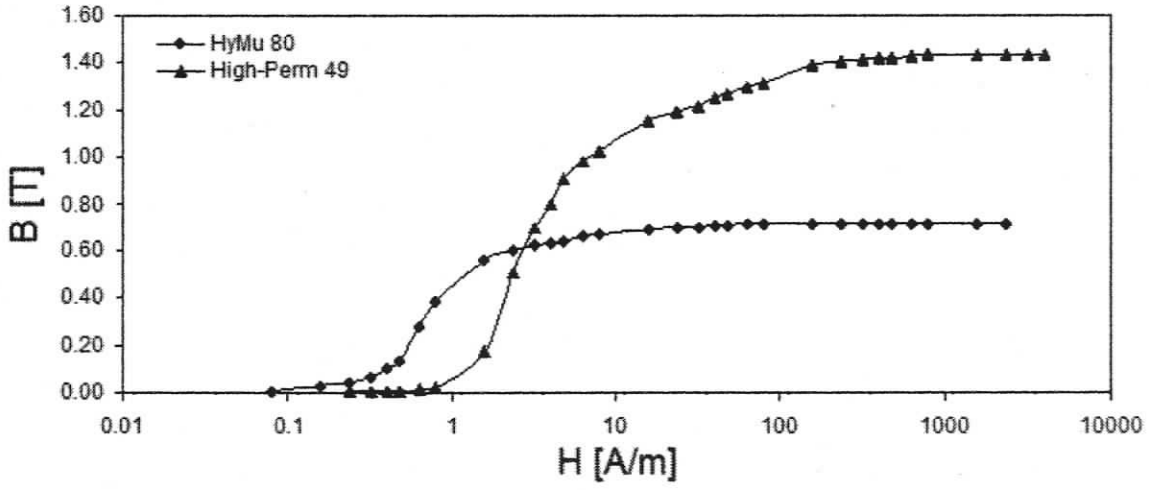

Figure 2-4: B-H curves for Hymu 80 and High-Perm 49 [4]

2.2.3 Low Temperature Effects on Ferromagnetic Materials

Another important property of a ferromagnetic material is the Curie temperature, T_C. Above the Curie temperature a ferromagnetic material becomes paramagnetic. This temperature is typically above room temperature for materials of interest such as nickel (631 K) and iron (1043 K)[3]. The Curie temperature of Hymu 80 is 733 K while that for High Perm 49 ranges from 722 K to 772 K. [4] The behaviour of many ferromagnetic materials with decreasing temperature is generally as shown in Figure 2-5. The Saturation Magnetization increases rapidly in the temperature region just below the Curie temperature T_C, and continues to rise at a slower rate with a continued temperature decrease. This is due to decreasing thermal agitation of the spin system with decreasing temperature [3].

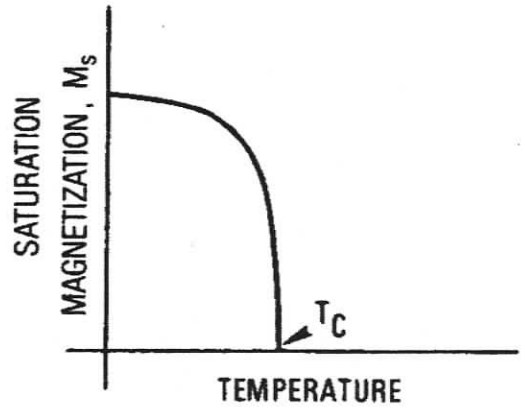

Figure 2-5: Saturation magnetization vs. temperature [3]

Since most materials of interest, including the materials from which the clamps are manufactured, have high curie temperatures, the change in saturation magnetization between room temperature and 4k is seldom more than 10% [3]. However, a 10% increase in clamp performance would be significant. Other properties such as permeability and remanence can vary more drastically and can also influence the performance of the clamps [3].

2.2.4 Maxwell Stress Tensor

The Maxwell Stress Tensor is one method commonly used in FEA analysis to calculate the electromagnetic forces on a body. Integrating of this stress tensor S over any surface in vacuum enclosing a body will give the net force on it directly [5]. The electromagnetic force as derived from the stress tensor is described by equation (2.10).

$$F = \iint (S \cdot \vec{n}) dA \tag{2.10}$$

Where n is the unit normal vector [5]. Components of the magnetostatic tensor S are shown in equation (2.11)

$$S = \frac{1}{\mu_0} \begin{pmatrix} B_x^2 - \frac{B^2}{2} & B_x B_y & B_x B_z \\ B_y B_x & B_y^2 - \frac{B^2}{2} & B_y B_z \\ B_z B_x & B_z B_y & B_z^2 - \frac{B^2}{2} \end{pmatrix} \tag{2.11}$$

By evaluating the dot product between S and n, the explicit form of the integral can be found. [5]

$$F = \frac{1}{\mu_0} \iint \left[(B \cdot n) B - \frac{1}{2} B^2 n \right] dA \tag{2.12}[5]$$

Integrating equation (2.12) around a surface enclosing an object gives the net magnetic force on that object. This integral can be used in FEA post processing to predict the magnetic forces between two objects such as the clamp jaws.

2.2.5 Lorentz Force Law

The Lorentz Force Law describes the force exerted on a charged particle which is moving in an electric or magnetic field and is described by equation (2.13)

$$\vec{F} = q\left(\vec{E} + \vec{v} \times \vec{B}\right) \tag{2.13}$$

Where q is the charge of the particle, E is the electric field, B is the magnetic flux density and v is the velocity of the particle through the fields. When only magnetic fields are considered, the equation can be simplified to the form shown in equation (2.14)

$$F = q\left(\vec{v} \times \vec{B}\right) \tag{2.14}$$

Current traveling through a wire is in effect made up of several moving charges. Therefore a current carrying wire immersed in a magnetic field will experience a force exerted on it by the interaction of the charges passing through it and that field. The force exerted per unit length of such a wire can be determined using equation (2.15)

$$\frac{d\vec{F}}{dl} = \vec{i} \times \vec{B} \tag{2.15}$$

The vector form of i has the same magnitude of the scalar value of i and has a direction equivalent to the direction along the wire. The direction of the force on the wire is described by the cross-product but can be determined using the Right Hand Rule and is perpendicular to both the magnetic field and the current vector. Equation (2.15) shows that the force on a wire is directly proportional to its immersed length, the magnitude of its current as well as the magnitude of the field in which it is immersed. The length of the wire immersed in the field can be increased by looping the same wire through the field several times.

2.3 Finite Element Clamp Geometry Simulations

During simulations, the clamp design was modified from the original design by altering the following parameters:

- Coil aspect ratio
- Upper clamp leg height
- Upper clamp bar leg width
- Material
- Coil current

A brief description of the variations of these parameters is given in Appendix A.

To determine which clamp design will be the most promising, a series of models were analyzed using FEA software. FEA software approximates partial differential equations by replacing continuous functions by piecewise approximations defined on polygons [6]. The polygons divide the problem into small sub-domains, or elements, and calculations are performed at each intersection between elements. These intersections, called nodes, take into account the results of adjacent nodes resulting in a continuous solution across the area or volume. The collection of elements which divide a problem is commonly referred to as a mesh. Models can contain several thousands of elements and may require significant computational resources and can only be practically solved using computers.

Ideally the MARS electromagnets would be analyzed in three dimensions but the preliminary clamp analysis can be achieved using a two-dimensional approximation. This approximation can be used to identify clamp geometries which provide increased clamping performance. Using the two-dimension model greatly reduces the amount and complexity of calculations needed and reduces the computation time significantly.

2.3.1 Problem Setup

The 2D approximation of the clamps neglected the clamp thickness and assumed that the material was very large in this dimension. The coil was approximated using two regions which represent its cross section. Figure 2-6 shows the cross-section of the clamp

assembly while Figure 2-7 shows the FEA approximation. The clamp bars are identified as Hymu80, which is one of the alloys used for the clamps. The other regions are labelled as copper and air for the coil and surrounding environment respectively. From these two figures it can be seen how the coil current is represented in the two-dimensional model. The two coil regions in Figure 2-7 labelled "*Copper [coil current in*]" and "*Copper [coil current out]*" are both parts of the virtual coil. To simulate a current of 50 mA through a 420 turn coil, the value for "coil current in" was set to 21A, while the value of "coil current out" was set to -21A.

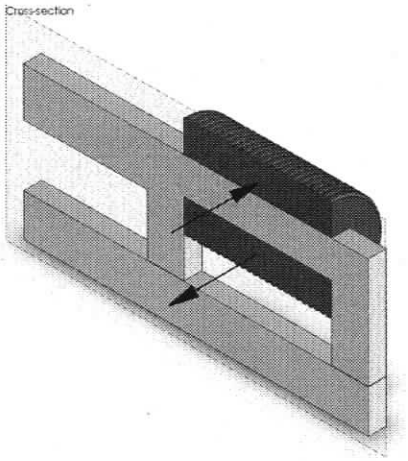

Figure 2-6: Cross section of clamp showing coil currents

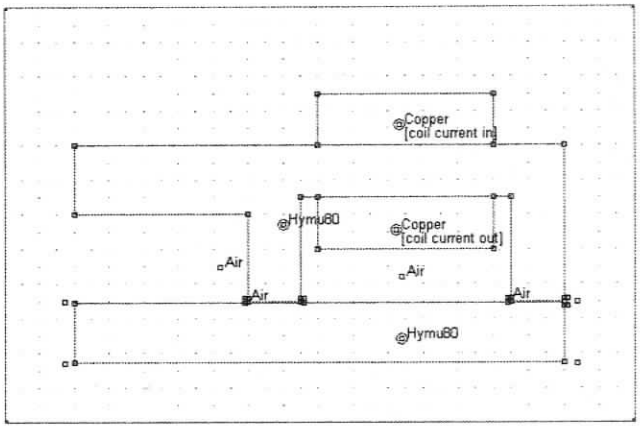

Figure 2-7: FEA model showing the clamp bar and the coil regions

One of the problems with the two-dimensional model is that it represents planar symmetry. Planar symmetry assumes infinite dimension in and out of the page. It was decided that this inaccuracy is acceptable for the clamp simulations since their main focus is to determine the 2D geometry which yielded the highest flux density in the gap. The model was defined to have a depth of 1mm. Although the original clamp design is 3mm deep, using 1mm as the depth of the simulation gives results which are in units of N/mm which can then be multiplied by any depth to give the total clamping force.

Since the flux density across the gap is integral for calculating the clamping force, steps were taken to improve the accuracy of the FEA calculations in those regions. With a relatively sparse mesh density, the program places a mesh in the gap which consists of

one row of triangular elements bridging the gap. This could lead to inaccuracies in calculations since the flux density would be modeled as constant across the gap. To improve the accuracy of the gap calculations, a region was set up around the gaps with a smaller mesh size. As mentioned, the relative permeability of most nonmagnetic materials, including air, is equal to 1. Since the shutter material will be a nonmagnetic material, it was acceptable to use air in the simulation to approximate the material between the gaps.

Once the model was completed, the results were used to calculate the force acting on the lower bar. A path was defined which completely enclosed the bar and the Maxwell stress tensor is integrated along this closed path to determine the net force. Another property which was determined from each simulation was the flux density at the center of the coil core. This parameter indicated whether the material had reached magnetic saturation. It was also useful for plotting the effect of increasing current on the clamps performance.

2.3.2 Results of Clamp Shape Experiments

The clamping force results of several clamp geometry models are shown in Figure 2-8. It can be seen that there is negligible difference between the performances of Hymu 80 and High Perm 49. Geometry #21 had the greatest performance for a Hymu 80 based clamp with a clamping force of 0.405 N/mm. For the High-Perm 49 clamps, geometry #16 had the highest performance with a force of 0.442 N/mm. For the same geometry Hymu 80 show similar performance but generated ~9% less clamping force at 50 mA coil current.

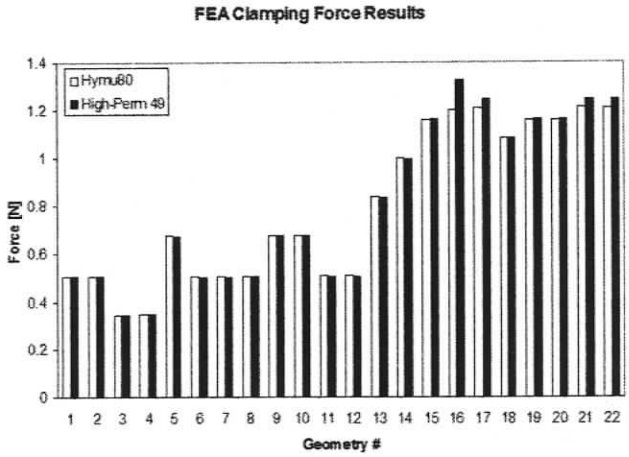

Figure 2-8: Results of force calculations for High-Perm 49 and Hymu 80

Geometry #16 varies from the original clamp design in that it has a longer, narrower coil which is 8 mm in diameter and 12 mm long as opposed to the 10 mm diameter and 10 mm length of the prototype. In addition to the coil aspect ratio, geometry #16 has upper bar legs which measure 8 mm x 4 mm (W x H) as opposed to the prototype which has legs which measure 3 mm x 6 mm.

2.3.3 Results of Current Tests

In order to discover the effect of coil current on the clamping force, a series of simulations were performed on a single clamp design. Geometry #19 was chosen because of its relatively high performance and because it was a simple, symmetrical shape. The current through the coil was increased in regular intervals from 0 A until saturation was achieved. The clamping force and flux level at the center of the coil were recorded for each simulation. Figure 2-9 illustrates the results of this simulation. The x-axis represents the total current through the clamp cross section and is equal to I_{CC} multiplied by the 420 turns in the coil. It can be seen that Hymu80 reached saturation at a relatively low coil current. It can also be seen that the High-Perm 49 is capable of significantly higher forces than Hymu 80 but only at higher coil currents. This is especially evident when the current is greater than 25A. This behaviour is due to the high saturation flux density of the High-Perm 49 material.

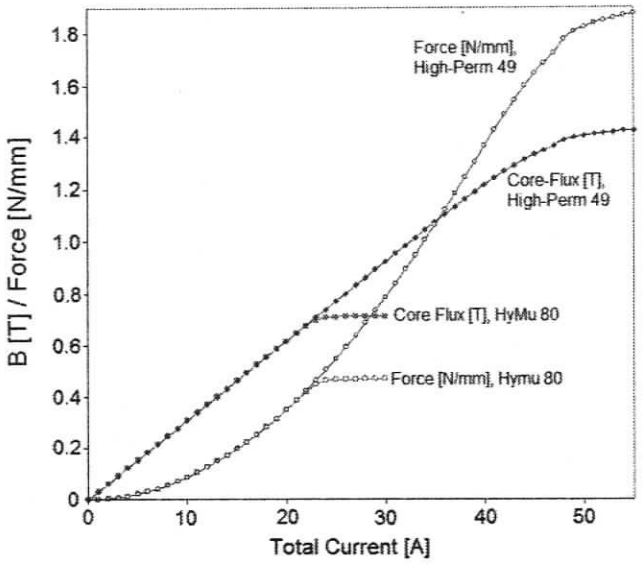

Figure 2-9: Clamping force and core flux density versus coil current for Hymu 80 and High-Perm 49 (geometry #19)

In order to illustrate the effect of increased current on the prototype clamp (geometry #1) the coil current experiment was repeated. The simulation was performed on the original design using Hymu 80 and compared with the data for model #19 using the same material. Figure 2-10 illustrates the results of the simulation. It can be seen that the original design has a maximum clamping force that is nearly double that of model #19. However, #1 requires nearly twice the current to achieve its maximum force. Also, in the lower current range, #19 has approximately twice the clamping force of #1. It can also be seen that #19 reaches saturation at a much lower current. This is important when considering the heat load as discussed in section 2.1.

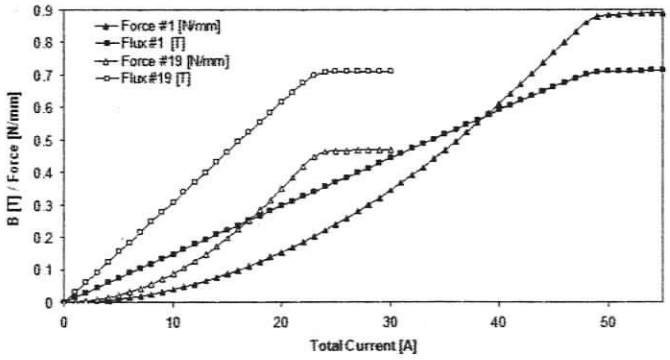

Figure 2-10: Clamping force and core flux density vs. coil current for both model #1 and #19

2.3.4 Analysis of FEA Results

The results of the FEA simulations reveal that High-Perm 49 is the preferred material for the MARS device's magnetic clamps. The High-Perm 49 clamping forces are, on average, stronger than the Hymu 80 clamps. The higher performance High Perm 49 clamps are as much as 10% stronger than their respective Hymu 80 clamps. This is not unexpected as High-Perm saturates at a much higher flux density than Hymu 80. A strong correlation between the width of the clamp legs and the clamping force is observed. It is also noticed that the flux density in the core of the clamp increased with the leg width. The magnetic circuit calculations discussed in section 2.2.1 showed that the air gap is the prime source of reluctance in the circuit. Since the reluctance of an air gap is inversely proportional to it's cross sectional area, the reluctance of the circuit is reduced with the increase in leg width. This in turn would increase the flux density in the circuit and consequently, the clamping force.

Another method of increasing the total flux in the gap is to increase the current in the coil. The total current can be increased by either increasing the wire current or by adding more windings to the coil. Both methods lead to an increase in heat generation. The heat generated by the coil is defined by the relationship outlined in equation (2.1). Increasing the coil current, I, produces a quadratic increase in heat generation while increasing resistance R via the number of windings increases heat generation linearly. However, additional windings would also increase the cross-sectional area of the coil which would be counter productive to the goal of the design.

Experiments #16, #18, #21 and #22 show the best results of all 22 simulated. For the High-Perm 49 clamps #16 is 63% stronger than the original design and has the potential to be even stronger, as discussed above. For the Hymu 80 clamps, #21 is the strongest with 39% more clamping force than the original design. However, #17 has a simpler design and will be easier to incorporate into the test apparatus. #17 is only marginally weaker than #21 and has 38% more clamping force than the original design. Of all the clamps simulated, the maximum force is found to be 0.44 N/mm which for a 3 mm thick clamp gives a clamping force of 1.33 N.

2.4 Summary

This chapter outlined all relevant theory which will be applied in the development and discussion of the components of an apparatus to be used to characterise the MARS clamps. In addition to the theory presented, the preceding simulations showed that the maximum expected clamping force deliverable from the MARS clamps is 1.33 N. This means that a test apparatus must be capable of exerting at least 1.33 N of force. This will be used as a baseline for the development of the test apparatus. All information needed for the apparatus design has now been put forward. The following chapter will discuss further simulations and models which are intended to determine the experimental method.

Chapter 3 Test Apparatus Component Modeling

3.1 Cryostat and Heat Shielding

The cryostat was developed and built to accommodate several experiments including the MARS project. It was designed to allow easy access to experimental apparatuses and to be adaptable to many diverse experiments. The main structure consists of an aluminum pressure vessel which houses a single stage Gifford McMahon (GM) cryorefrigerator. The GM refrigerator has, as part of its operation, a reciprocating displacer which oscillates inside a steel cylinder. The motion of this displacer induces vibrations in the chamber which can significantly interfere with the accuracy of test results. It is necessary to develop a method of isolating the test apparatus from these vibrations.

Measurements of system vibrations were obtained using a displacement based measurement system. The vibration was found to have a primary frequency of 2.4 Hz which corresponds to the frequency of the main displacer. The main amplitude of vibration is 0.023 mm. Intuitive observation of the level of vibration put the success of an isolation system into doubt. Because of this, it was decided that such a system would be too complicated and time consuming to pursue. Instead the simpler solution of performing the force measurement experiments with the cryorefrigerator deactivated was employed. This removes all vibrations and allows for accurate force measurements.

Since the experiments are performed with the cryorefrigerator inactive, it was necessary to minimize the heat flow into the system. To achieve this, several experiments were performed which were designed to determine the amount of time that would be available for experiments and the best method to extend that time. These experiments monitored the temperature of the test area and record the time required for the temperature of the system to rise from 20 K to 65 K. This value is given the notation $t_{20\text{-}65}$. This temperature range was chosen to include the desired operating temperature of 30 K as well as a satisfactory temperature range above and bellow that temperature. The rise time for the

smaller, more pertinent temperature range of 25 K to 35 K is determined from the same results. This value is given the notation $t_{25\text{-}35}$.

The first experiment established a base-line for subsequent experiments. This experiment recorded the temperature rise at the top of the cryorefrigerator with no radiation shielding or thermal mass added to slow the warm rate. The second experiment involved the addition of a multilayer insulation (MLI) heat shield which was thermally linked to a point on the cryorefrigerator approximately half way between the cold tip and its base. This point was previously found to reach an equilibrium temperature of ~140 K. The third experiment closely mimicked the second in that the same shield was used. However, it was thermally sunk to the top of the cold head instead of the bottom. The forth experiment was performed by first returning the system to the base-line condition by removing all heat shield equipment. A 1.18 kg copper disk was added to the top of the cold head. The thermal mass was added so that incoming heat is consumed in the heating of a larger mass thus slowing the temperature rise. The mass used was a disk 7" in diameter and ¼" thick with a 3" hole in the center to accommodate a heater. The results of all four experiments show that the bottom-sunk heat shield out performs the top-sunk shield. It was also shown that the addition of thermal mass greatly reduced the temperature rise rate.

Using the information gained from these experiments, a final cryostat configuration emerged. The thermal mass of the system was increased by adding a copper plate to the top of the cold head. Additional thermal mass was added as part of a radiation shield. The shield consisted of a cylindrical copper structure which was thermally sunk to the bottom portion of the cold head. This cylinder was wrapped on all sides with MLI blankets comprised of 22 – 30 layers. A small opening in the top of the heat shield was included to allow for viewing of the experiment via a view port on top of the cryo-stat. The final configuration was tested in the same manner as all previous experiments. Using this configuration, the value of $t_{20\text{-}65}$ was increased to 57:18 while $t_{25\text{-}35}$ was increased to 6:02. The results of all temperature rise rate experiments are shown in Table 3-1.

Table 3-1: Warm-up experiment results

			Improvement over base line	
Experiment	t_{25-35}	t_{20-65}	t_{25-35}	t_{20-65}
Base-line	2:04	25:09	0:00	0:00
Bottom sunk heat shield	2:35	30:37	0:31	5:28
Top sunk heat shield	2:17	28:46	0:13	3:37
Copper thermal mass	2:20	27:47	0:16	2:38
Final configuration	6:02	57:18	3:58	32:09

3.2 Problem Description

Figure 3-1 shows the chamber used for the experiments. During experiments, the environment inside consiste3d of an ultra high vacuum and temperatures which ranged from room temperature at the outer wall to 30 K at the cold plate where the clamps were mounted. The chamber was primarily constructed from Aluminum and although it was quite large, allowed limited space for the measurement device. As described in the previous section, the interior of the chamber included a cylindrical radiation shield. This shield was constructed from copper and was covered by several layers of super insulation blankets to reduce the radiative heat transfer between the cold interior and the warm outer walls of the chamber. In order to ensure that the measurement hardware remained at room temperature and to ensure that its operation did not interfere with the cooling of the clamp, it was necessary to have the device outside the radiation shield but inside the outer wall.

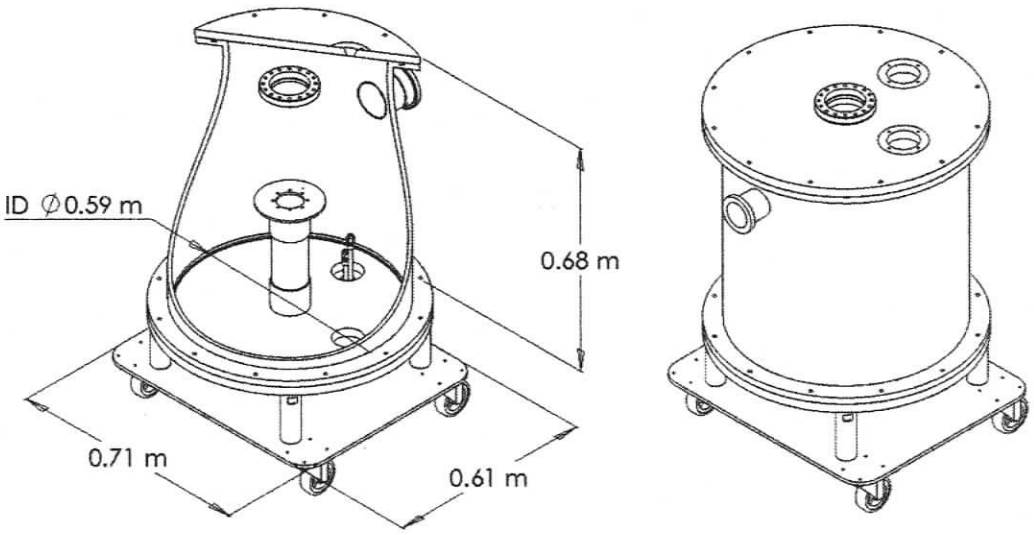

Figure 3-1: Cryogenic chamber to be used for testing

Since the high vacuum operating conditions inside the cryostat leave only conduction and radiation as possible heat transfer modes, the force measurement apparatus must be mounted to the inside surface of the outer wall. In this location, conduction occurs from the chamber walls to the apparatus while radiation heat flow occurs from the apparatus to the internal cold surfaces. Since it is desired to keep the hardware at near room temperature, good thermal contact between it and the chamber wall is required in order to maximize the heat flow between them and good radiation shielding is needed to keep the heat flow to the cold surfaces to a minimum.

Conventional measurement devices such as load cells, strain gages and piezoelectric sensors merely measure the magnitude of an externally applied force. They do not apply the force themselves. Although piezoelectric transducers can perform both tasks, they are prohibitively expensive. The enclosed nature of the cryo-chamber requires that a variable force be adjustable remotely by the user from outside the chamber. An ideal device would be able to act both as a force measurement device as well as the source of the applied force. The proposed solution to this problem takes advantage of the Lorenz Force generated on a current carrying wire in a magnetic field. By varying the magnitude of the current through the magnetic field, the applied force can be both controlled and quantified. Both proposed design solutions consist of two main components, the force coil and the field generator. A Helmholtz coil pair and a permanent magnet assembly are both considered for generating the magnetic field in which the force coil is suspended.

3.3 Literature Review Force Measurement

Before development of a measurement system began, a search of current techniques was performed. A thorough search of journal databases as well as internet search engines yielded few methods to the problem of measuring small forces in a cryogenic environment.

One method was developed for cryogenic force measurement at the Miyagi University of Education in Miyagi Japan [8]. The apparatus used the pendulum effect to measure the

repulsive force between a solenoid coil and a superconducting film. The research was intended to study an actuation method for fringe lock interferometric gravitational-wave detectors. The actuation method employed the repulsive force experienced by a superconductor subjected to a magnetic field. The magnitude of that force could be adjusted by controlling the current through a solenoid coil which generated the magnetic field.

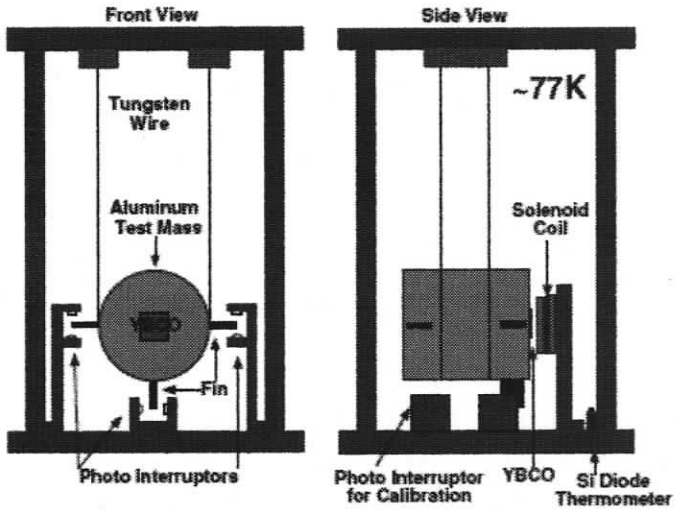

Figure 3-2: Miyagi University test apparatus diagram [8]

The experimental apparatus, shown in Figure 3-2, used a test mass which was suspended by tungsten wires inside a cryostat. The superconducting film was bonded to one face of the test mass using epoxy glue. The solenoid was placed such that it could exert a magnetic field on the surface of the superconducting film. The position of the test mass was determined by monitoring the output of three photodiodes placed at the sides and bottom of the test mass. Fins mounted to the test mass interrupted the light output from LEDs which illuminated the photodiodes. The displacement in the x-direction was used to calculate the repulsive force by using the pendulum equation given by equation (2.16)

$$F_Z = \frac{mg\Delta z}{l} \tag{2.16}$$

Where F_Z is the force and Δz is the displacement, both in the z-direction, and l is the length of the pendulum wire.

This system of force measurement would not be suitable to the MARS experiments as they require that a force be applied to the clamps. This apparatus simply measures the repulsive force applied to it by a magnetic field, it cannot generate the force on its own.

Another potential system uses a suspended mass to apply a constant load on a test plate. The apparatus is part of a test rig for characterizing wear on ball bearings intended fro cryogenic fuel pumps in rocket motors. A loading pan is over-hung on a pulley with balancing dead weight, which maintains a constant normal load condition throughout the test. This kind of loading arrangement ensures a constant load during dynamic conditions of repeated sliding wear tests [9]. This method of applying load to an object is ill suited to the MARS experiments because the load is constant.

Franz Keplinger et al. developed a sensor which uses the principle of Lorentz force to detect the strength of a magnetic field. The Lorentz force is proportional to the magnetic flux density and to the electrical current on the cantilever. [10] This means that the force generated on the coil can be precisely controlled by varying the magnitude of the current passing through it. The application of the magnetic field sensor used only a single conductor passing through a magnetic field. The conductor was micro-machined on thin wafers. For the MARS experiments, the conductor can be increased in size wound into a coil which can increase the magnitude of force generated significantly. This method can be used to apply a know force to the MARS clamps remotely.

3.4 Force Measurement Method

In order to characterise the holding force of a clamp, a method of applying a known force to them is needed. One possibility is to suspend an attachment from a jaw and slowly add mass until the jaw is forced open. This simple solution is impossible to perform inside a cryostat because of its enclosed nature and extreme environment. Because of this, it is necessary to devise a remotely operated apparatus which could apply and measure a load on the clamp jaws. Requirements for such a device include that it be as small as possible to fit in the limited space available and generate as little heat as possible to reduce its

impact on the cold surfaces of the cryostat. Two systems were devised, both of which employ the Lorentz Force but differ in the method used to generate the necessary magnetic field. This chapter will present designs for the force actuation mechanisms and analyze their performance using simulations.

The two devices were modeled using FEA software to characterize magnetic field intensity as well as the forces generated on a current carrying coil used with each field generation method. Two FEA modeling methods were employed. First, simple 2D models were used to determine the magnetic field inside the two field generators. The second method used 3D models to compute electromagnetic forces on the force coil inside the magnetic field for both field generator configurations. Once each FEA analysis was completed, the data was postprocessed to yield the net force on the coil. This could be achieved by a number of methods but for this exercise the best method was integrating the volume force shown in equation (2.17). This is the most important method for computing forces in current carrying devices [7]. This method integrates the force given in equation (2.15) over the entire volume of the force coil.

$$\vec{F} = \vec{J} \times \vec{B} \tag{2.17}$$

3.5 Proposed Measurement Technique

The general principle of the proposed force measurement system is shown in Figure 3-3. The system works on the principle of the Lorentz force experienced on a current carrying conductor immersed in a magnetic field. The main components of the system are numbered 1 through 3.

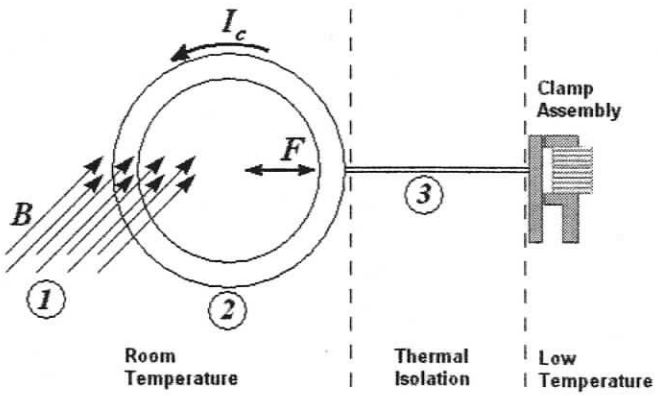

Figure 3-3: General actuator components

The magnetic field B (1) will be provided by a field generator. The important characteristics of this component are that it be capable of providing a large, uniform flux in a usable volume and that it be compact. The force coil (2) is used to carry the current I_c which passes through the magnetic field thus generating the Lorentz force F. The important characteristics of the force coil are that it provide the maximum current density and the minimum total electrical resistance. The latter will ensure that the heat generated by the coil is kept to a minimum. The force link (3) will act as a mechanical link between the force coil and the clamp jaw. This component must be rigid but thin in order to minimise the heat conduction from the warm force coil to the cold clamp assemble. The force coil and field generator will be kept at room temperature while the clamp assembly is at cryogenic temperatures. The force link will be between the two zones and will act as thermal isolation between them. The following section will discuss the methods of generating the magnetic field. The two proposed methods are permanent magnets and Helmholtz coil pair as shown in Figure 3-4.

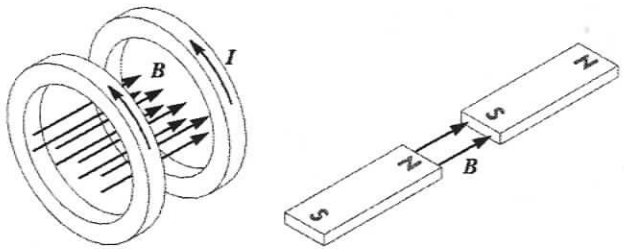

Figure 3-4: Two options for field generator design

The permanent magnet based field generator is discussed in section 3.6 while the Helmholtz coil pair is discussed in Appendix B.

3.6 Permanent Magnets

Permanent magnets are a cheap and effective means of generating powerful magnetic fields over small volumes of space. One common permanent magnet material is sintered Neodymium-Iron-Boron ceramic (NdFeB). NdFeB magnets, known as rare-earth magnets, are among the strongest permanent magnet materials currently available. NdFeB is also readily available in a variety of shapes, sizes and strengths. These standardized shapes can be combined together to build complex magnetic circuits. For

the purposes of the field generator, a C-shaped magnetic circuit with a wide region of high magnetic field in the gap is required. Figure 3-5 shows two possible configurations of the plate style magnets. The light coloured portions on the magnet are stacked NdFeB magnet plates while the darker portions are composed of a soft magnetic material, such as iron which acts as a flux return path for the magnetic circuit. The configurations shown are intended to determine the effect of variable amounts of magnetic material in the circuit.

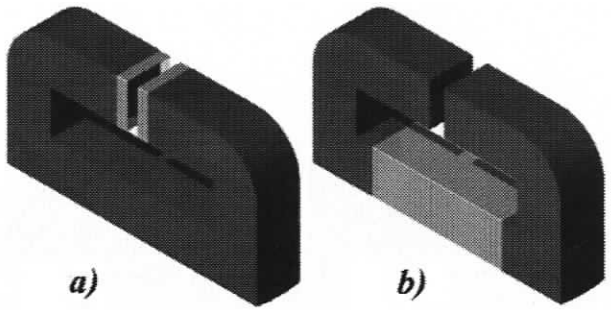

Figure 3-5: Two possible permanent magnet configurations, a) Top Stacked b) Bottom Stacked

The FEA simulations of the permanent magnet field generator analyzed the used of 3.2 mm thick NdFeB plate magnets in stacks to improve the performance of the field generator. One configuration used magnets stacked in the bottom of the field generator, and is hereafter referred to as "bottom stacked". The other configuration used magnets stacked at the top of the field generator and is hereafter referred to as "top stacked". In order to allow quick addition of magnet plates to the simulation, the field generator was modeled as seen in Figure 3-6. The segmented portions seen in the figure mimic stacks of individual blocks, each representing a standard sized magnet plate. These blocks could be switched between representing a magnet or piece of flux return simply by adjusting their properties in the FEA software. When the blocks were deactivated, they were given the properties of iron while when activated are given the properties of NdFeB magnets. The remainder of the model represents the iron flux return structure which concentrated the field in the air gap at the top of the field generator.

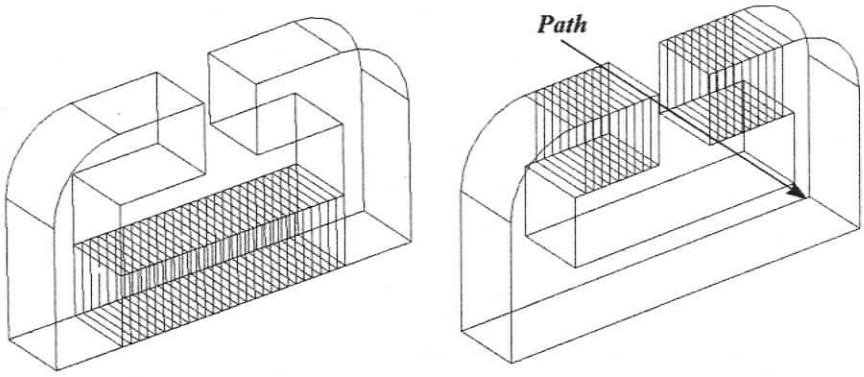

Figure 3-6: FEA models of bottom and top stacked permanent magnet field generators

Permanent Magnet Field Strength Simulations

The first simulation involved only the middle magnet of the *bottom stacked* configuration being activated. All 26 of the other magnets were set to emulate iron as are the flux return portions of the model. The resulting flux density is plotted on a path through the center of the gap as shown in Figure 3-6 and is shown in Figure 3-7. This procedure was repeated for the addition of magnets, two at a time, to a total of 27 magnets stacked together on the bottom portion of the field generator.

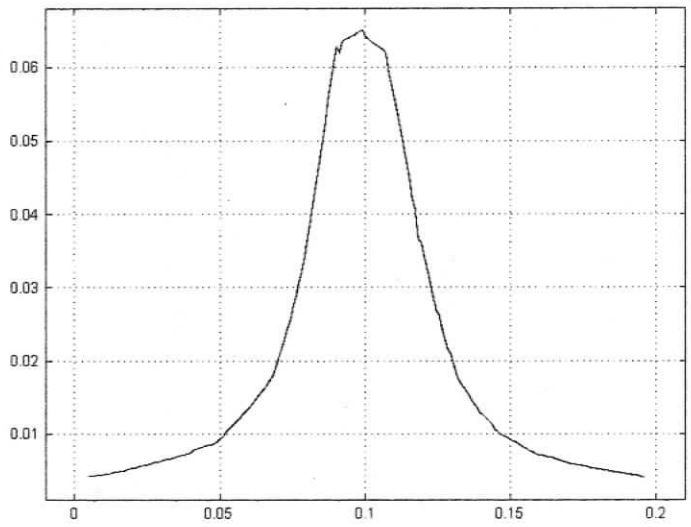

Figure 3-7: Flux density, B, through the gap of a one magnet field generator

The same experiment was repeated for the field generator with the magnet plates stacked on the top bar, directly adjacent to the gap. The same modeling procedure was followed and all other conditions were left the same. The peak flux density values of each test are plotted in Figure 3-8. It can be seen that the top mounted magnets produce a higher flux density in the gap than the bottom mounted. The field generator with the top mounted magnet plates yielded better performance with two magnets than the bottom mounted generator did with twenty seven. After several re-evaluations of the model and further investigations it was determined that this was due to the size of the gap. When the gap was made smaller the field strength grew. Limited simulations were performed to explore this property since the gap width must remain relatively large in order to accommodate the force coil.

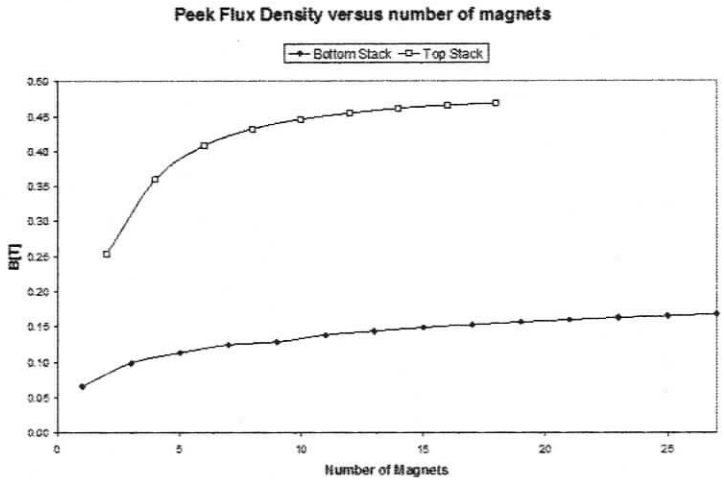

Figure 3-8: Peek flux verses number of magnets for both the top and bottom stacked field generators

In addition to the top and bottom stacked field generators, other configurations were simulated. Configurations which used both top and bottom stacked magnets as well as configurations with magnets stacked on the vertical portions of the flux return yolk were included. Also, a top and bottom stacked field generator was simulated which has twice the depth as the other models.

It was found that the bottom stacked field generator is the weakest while the top stacked is significantly stronger. A combination of top and bottom stacked magnets resulted in a

small improvement in performance where as the addition of magnets in the vertical side bars does little to improve the magnets performance. The best results were noticed when the depth of the magnet is doubled to 50.8 mm. Not only is the peak flux density much stronger, but the region of high flux is much wider than with the 25.4 mm wide generators

3.6.1 Permanent Magnet Force Simulations

Force simulations were time consuming due to the increased complexity of the models and the additional calculations necessary. Where the field test simulations could be computed using a simplified magnetostatics application mode, the force simulations required the presence of a current carrying coil which required that the FEA software use a more complex application mode. This, coupled with the increased number of elements due to the force coil model, resulted in simulations which required several hours to compute. Because of this, it was necessary to simplify the process. The current density through the force coil was varied from zero to the maximum. Each current density change required that the model be recomputed. This could take as long as 6 minutes per change and with dozens of computations necessary, the simulations could take several hours.

The magnitude of the current density could be altered after a simulation completed and a "model update" could be performed. Updating was an alternative to recomputing the model after every alteration. Updating only took seconds to compute compared to the 6 minutes required for a full simulation but was flawed since it did not take into account the effect of the force coil current on the magnetic field. To determine the amount of error, one configuration was simulated using the shortened process as well as by running a standard calculation for each current density. A simulation of the system was conducted with a force coil current density of zero. This established a base-line flux density distribution which will be called B_0. Using this base line, the force is calculated by varying the current density up to the maximum as shown in equation (2.18).

$$F_0 = \bar{I} \times \bar{B}_0 \tag{2.18}$$

Once a F_0 vs. I curve was developed the actual force, F, was calculated by changing the current density and running a full computation for each iteration. The difference between these two values was taken and plotted in Figure 3-9. The maximum error is only 17.9 mN and corresponds with a coil force of 17.46 N which is an error of only 0.1%. It was decided that this error is acceptable for these simulations and the simplified method could be used to determine the force on all other configurations.

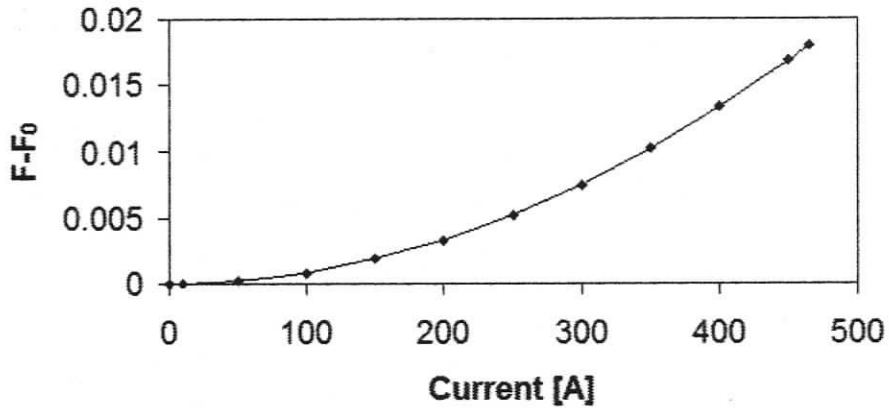

Figure 3-9: Error between F and F_0 for force coil current density from zero to maximum

Based on the findings outlined in previous sections four magnet configurations were chosen for simulation. These were:

1. Top and Bottom Stack, 25.4 mm deep with a 1 cm^2 force coil cross-section
2. Top and Bottom Stack, 50.8 mm deep with a 1 cm^2 force coil cross-section
3. Top and Bottom Stack, 50.8 mm deep with a 2.25 cm^2 force coil cross-section
4. Top Stack only, 50.8 mm deep with a 1 cm^2 force coil cross-section

The maximum force generated by configuration #1 is 3.94 N with 206.7 A/m^2 force coil current density while configuration #2 is able to generate 7.77 N with the same current density. Configuration #3 generates a maximum force of 17.4 N. There is no significant change in performance between configurations #2 and #4 which leads to the conclusion that it would be unnecessary to include magnets on the bottom of the field generator.

The 50.8 mm wide field generator (#2) out-performed the 25.4 mm (#1) significantly. The larger force coil increased the performance dramatically by allowing more turns of wire and thus a higher coil current within the high magnetic field zone. However the size of the coil is limited by the space available for it as well as the characteristics of the powers source used to drive it.

These simulations showed that a permanent magnet based field generator is capable of generating enough force to characterise the MARS clamp. The second field generator concept, the Helmholtz coil pair, would be unable to match the performance of the permanent magnets. Information on the study of the Helmholtz coil pair based field generator can be found in Appendix B.

3.7 Permanent Magnet Refinement

It has been shown that a field generator based on permanent magnets is capable of generating a magnetic field and force of sufficient strength to be used to characterise the MARS clamp. The simulations performed were based on the use of standard magnets which are readily available. Once the decision was made to use permanent magnets, further sources were explored and it was decided to use fewer, larger magnets which could be more easily handled. These magnets are designated as Grade 50 NdFeB magnets with a remanent flux density between 1.41 T and 1.47 T which is higher than the Grade 35 magnets used during the original simulations.

Further FEA simulations were performed in order to determine the optimum configuration of the magnets and the flux return yolk. The larger magnets have a length of 50.8 mm, a height of 25.4 mm and a depth of 12.7 mm. They are magnetized in the direction of the 12.7 mm side and were arranged such that the force coil would run parallel with the longest side as shown in Figure 3-10.

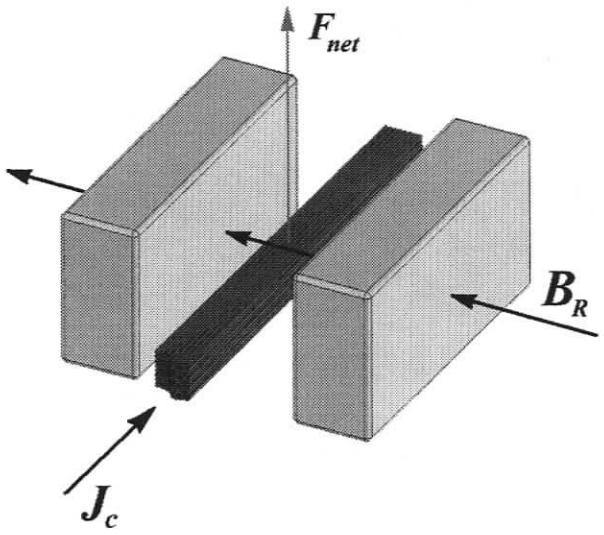

Figure 3-10: Permanent magnets arranged to produce maximum field through the force coil

This arrangement produced the same conditions of the 50.8 mm deep field generator simulated in section 3.6.1. To further increase the flux density in the gap, 6 additional magnets were added such that four magnets are arranged on each side of the field gap. This configuration is simulated with a 12.7 mm gap between each set of magnets. The flux density along a line centered through the gap is shown as a dashed line in Figure 3-11. The peak field strength is 0.73 T which is already stronger than the fields generated by the simulations in section 3.6.1.

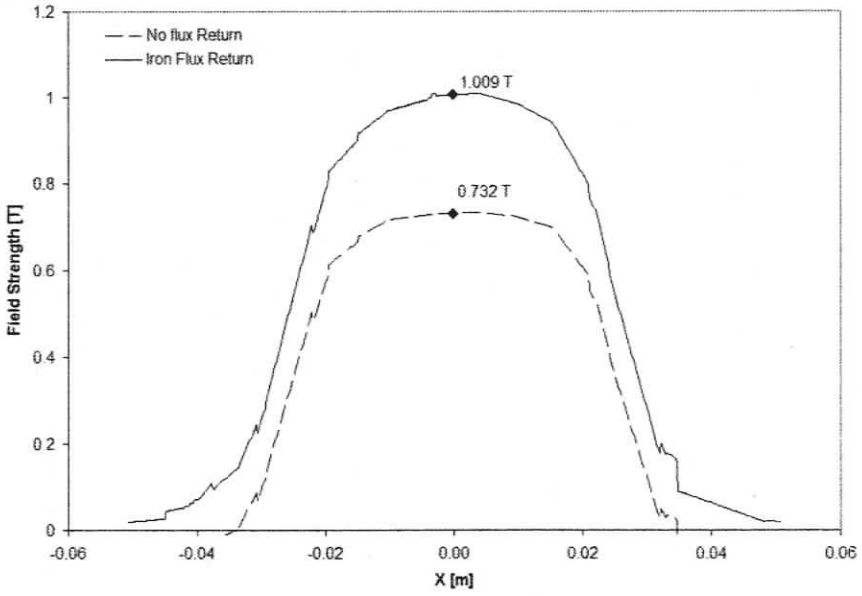

Figure 3-11: Flux density through field generator

The addition of a flux return yolk increased the field strength by channelling the magnetic flux back to the opposing set of magnets. The effect of the addition of a flux return yolk can be seen as a solid line in Figure 3-11. The flux density is plotted along the same path for each curve. It can be seen that the addition of an iron flux return increases the peak flux density to 1.0 T.

The permeability μ of a magnetic material affects the material's ability to channel magnetic fields. Several materials are modeled in order to determine if a more exotic magnetic material could offer a significant improvement over more readily available materials such as mild steel. The relative permeability μ_r of several steels, as well as the more exotic high permeability material called Mumetal, were each input into the FEA simulation. Figure 3-12 plots μ_r for each material against the magnetic flux density B. [6]

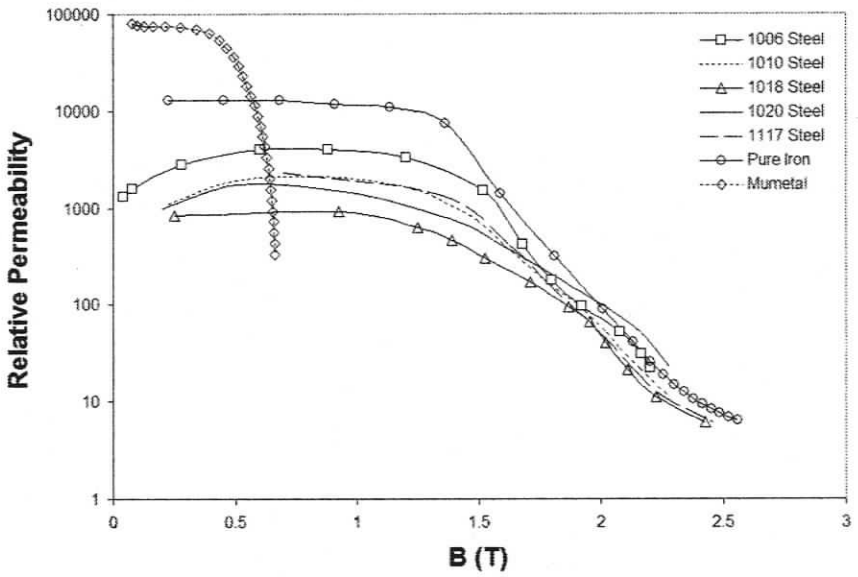

Figure 3-12: Relative permeabilities of several steels and other magnetic materials [6]

It is notable that Mumetal has a significantly higher μ_r at low levels of B but it saturates at a much lower flux density than the iron based materials. The results of the FEA models show that the material did not significantly affect the strength of the magnetic field in the

gap of the field generator. This is due to the fact that none of the materials simulated reach saturation when subjected to a field from the magnets.

3.8 Summary

This chapter outlined the problem of characterizing the MARS clamps. The development and testing of the cryostat heat shielding yielded a maximum time being available for performing experiments. An exploration of current techniques for force measurement or applying a load in an enclosed environment yielded few methods. However, a method using the Lorentz force was devised. Data collected from simulations was put forward and will be used in the design of the components described in the following chapter.

Chapter 4 Test Apparatus Development

4.1 System Components

The development of individual components of the clamp testing apparatus is described in detail in the following sections. The designs of these components are based on the analysis and research put forward in the preceding sections.

4.1.1 Field Generator

As described earlier, the magnetic field is generated using permanent magnets arranged in a magnetic circuit. The magnets used are constructed from sintered NdFeB and have a remanent flux density of 1.41 – 1.47 T. The field generator uses eight of these magnets. The design and refinement of this circuit was performed using FEA software. Several configurations were modeled in order to provide adequate field strength and uniformity. These FEA models were used to determine the shape and size of flux return that maximizes the field strength inside the circuit gap. The final design is shown in Figure 4-1.

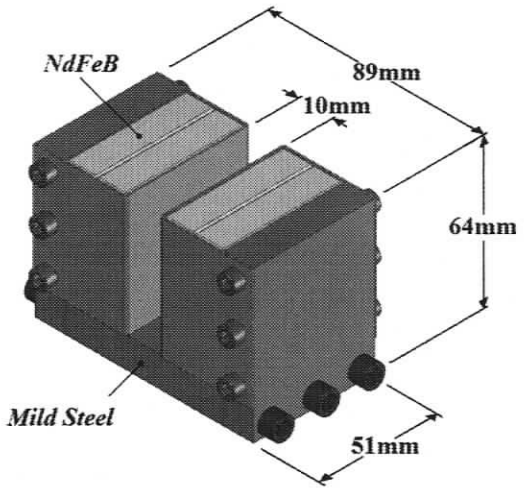

Figure 4-1: Final field generator design

This design includes three pieces of mild steel to form a flux return yolk and was chosen due to its simplicity and good performance. Simulations showed that this design provides excellent flux channelling and field strength in the field gap. The three pieces were

manufactured from mild steel bar stock and required minimal machining to complete. The eight magnets were mounted in groups of four on either side of the field gap and are held in place by magnetically inert stainless steel brackets.

4.1.2 Force Coil

The force coil is the second part of the electromechanical device which makes up the testing apparatus. The field generator supplies the magnetic field while the coil carries a current through it generating a known force. It is also the component which is mechanically coupled to the clamps themselves and exerts the load which is needed to force the clamp open.

The coil was designed such that it could be powered using a *National Instruments SCXI 1124* power output module for the DAQ system used. This module is capable of outputting a power signal with a maximum current of 20mA and a voltage range of 0-10 V. Because of the limited current available, the wire carrying this current was wound into a coil with as many turns possible in order to maximize the available force.

The size of the coil was limited by both the physical space available in the gap of the field generator as well as the coil's total electrical resistance R_c. This resistance was dictated by both the length of the coiled wire and the wire diameter. As stated, the DAQ module is capable of an output of 20 mA and 0-10V. Using a simple calculation of Ohm's law, the maximum resistance the coil could have is 500 Ω. This maximum resistance placed a restriction on the overall length of wire used. Therefore the coil had to be small enough to keep its resistance below this limit while big enough to allow the maximum number of wire turns. Another requirement of the coil was that it be large enough such that one side of the coil could be immersed in the magnetic field while the other remained sufficiently far away from the generator such that the magnetic force on that portion of the coil would be minimized. The reasoning for this requirement is more clearly illustrated in Figure 4-2. It can be noticed that the force generated in the left portion of the completely immersed coil is counter acted by the force generated on its

right side. The coil which is only partially immersed experiences a net force in one direction.

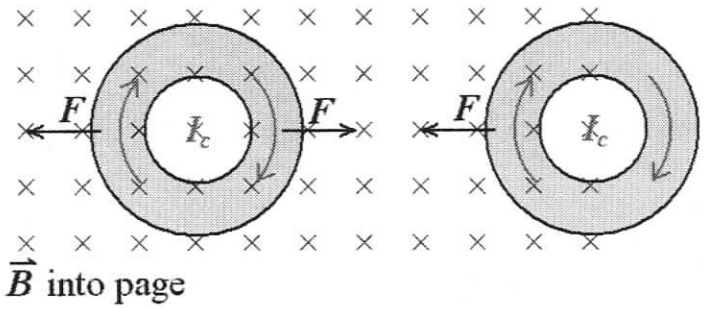

Figure 4-2: Magnetic forces on current carrying coils immersed in a magnetic field

Before the wire gauge and coil cross section was chosen, the shape of the force coil had to be determined. The final geometry attempts minimize the length of the coil wire while ensuring that only one side of the coil is immersed in the magnetic field. This geometry can be seen in Figure 4-3 and offers a short total coil length with adequate clearance for the portion of the coil which is to be free of the magnetic field.

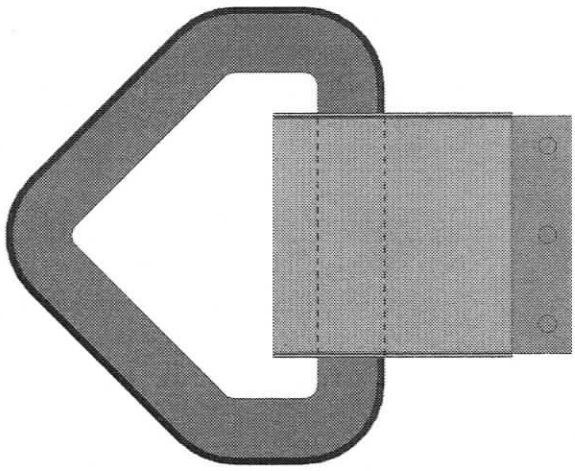

Figure 4-3: Final force coil design and its position in the field generator

In order to choose an appropriate wire diameter, several calculations were performed for various wire sizes using the final coil geometry shown above. In addition to these manual calculations, FEA models were created to estimate the theoretical force each wire

configuration would produce. The 20 mA which is deliverable from the DAQ module is not significantly high and can be handled by all wire thicknesses studied. However, the assumed maximum current for copper wire is taken from experiments performed at normal atmospheric pressure. In a vacuum there is no convection to remove heat from the wire so extra care must be taken to ensure a good conduction path for heat to be removed.

Table 4-1 shows the properties of three coils designed using each wire gauge. These three coils each used the geometry shown in Figure 4-3 but differed in their coil cross-sectional area. The columns of the table are defined as follows:

N is the number of turns and L is the length of wire needed to fill the coil
R_c is the coil resistance
F is the force determined using FEA simulations.

The top row gives the cross-sectional area of the coil modeled. The width of the coil was limited to 1 cm by the width of the gap in the field generator but the depth of the coil into the generator was variable up to 3 cm. The highlighted force cells denote configurations which yield 2 N or more. This is the minimum desired force which is chosen based on the FEA analysis of the clamps from section 2.3 plus a small margin. The highlighted R_c denote the configurations which do not exceed to the maximum coil resistance of 500 Ω.

Table 4-1: Coil data for coils constructed from each wire gauge

	1 cm^2				2 cm^2				3 cm^2			
	N	L [m]	R_c [Ω]	F [N]	N	L [m]	R_c [Ω]	F [N]	N	L [m]	R_c [Ω]	F [N]
36	6200	1449	2116	5.340	12400	3131	4571	10.644	18600	5280	7710	15.849
34	3906	913	838	3.365	7812	1972	1812	6.706	11718	3327	3056	9.986
32	2426	567	323	2.090	4853	1225	699	4.166	7280	2066	1180	6.203
30	1550	362	134	1.335	3100	782	290	2.661	4650	1320	489	3.962
28	918	214	45	0.791	1836	463	98	1.576	2754	782	166	2.347
26	597	139	19	0.515	1195	301	43	1.026	1793	509	72	1.528
24	383	89	8	0.115	765	193	17	0.657	1148	326	29	0.979
22	241	56	3	0.165	483	122	6	0.415	725	206	11	0.618

Although possible configurations in the 2 and 3 cm^2 coils developed the most force, they require excessive lengths of wire. These configurations were ruled out because of the impracticality of their construction. The coil configuration chosen has a cross sectional area of 1.5 cm^2 and is wound with 32 AWG copper wire. This configuration is not shown the table but was chosen based on interpolated data which yields a coil with a theoretical R_c of just over 500 Ω and a theoretical maximum force of 3.12 N. In order to ensure good thermal contact between the coil wires, the entire coil is saturated with epoxy glue during winding. This ensured that any heat generated in the coil would be dispersed away from the wires through conduction.

4.1.3 Adjustable Mount

During experiments, it was important that the test clamp be precisely aligned to the force coil which in turn must be aligned with the field generator. Because of this, it was necessary that the positions of each be highly adjustable. A mounting system which can hold the apparatus securely while allowing for adjustments in component position was required.

The final design for the mounting system is adjustable in 6 degrees of freedom, 3 transitional and 3 rotational. Figure 4-4 shows the complete mount system design with the field generator included transparent to better illustrate its position. The mount consists of two main sections each providing adjustment in three degrees of freedom. These components allow the magnet/force coil assembly to be precisely positioned such that it can be well aligned with the MARS clamp during testing. The coordinate system shown in the figure will be used in the following description of the mount operation as well as in following sections.

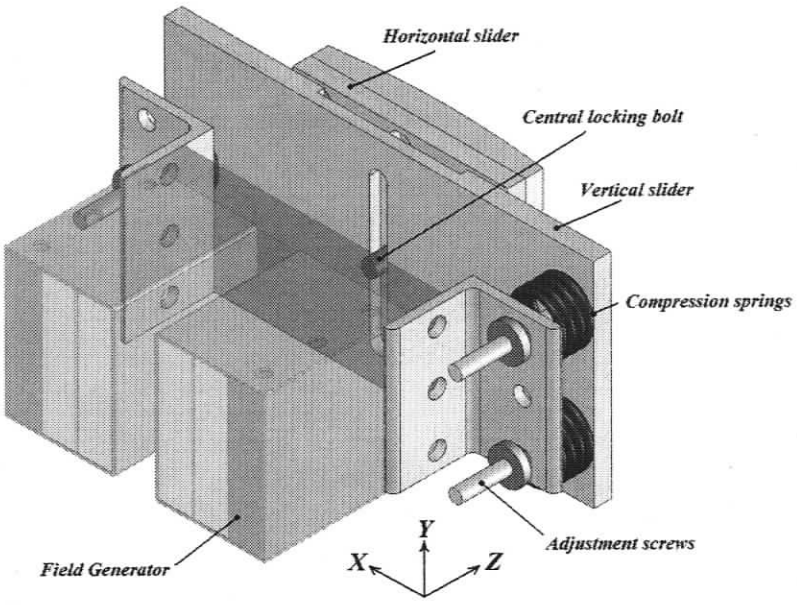

Figure 4-4: Complete mounting system with field generator

The first section, shown in the upper right hand portion of Figure 4-5, is made up of vertical and horizontal sliding components as well as a nylon disk which allowed it to rotate around a central bolt. The bolt is used to fix the assembly when the final position is obtained. This section provided translational displacements in the X and Y directions as well as rotational displacement about the Z-axis.

The second section of the assembly, shown in the lower left portion of Figure 4-5, consists of three compression springs which were used in conjunction with three threaded rods to adjust the position of two aluminum mounting brackets. The two brackets are bolted to the field generator such that it was fully supported by the three springs. By adjusting the screws on each spring the generator could be adjusted in the remaining three degrees of freedom. Adjusting all three screws equally translated the assembly in the Z direction while adjusting them in opposing directions resulted in rotation about the X-axis and Y-axis. The springs used are extremely stiff so that the field generator/force coil assembly could be held securely and minimal motion would occur due to external vibrations.

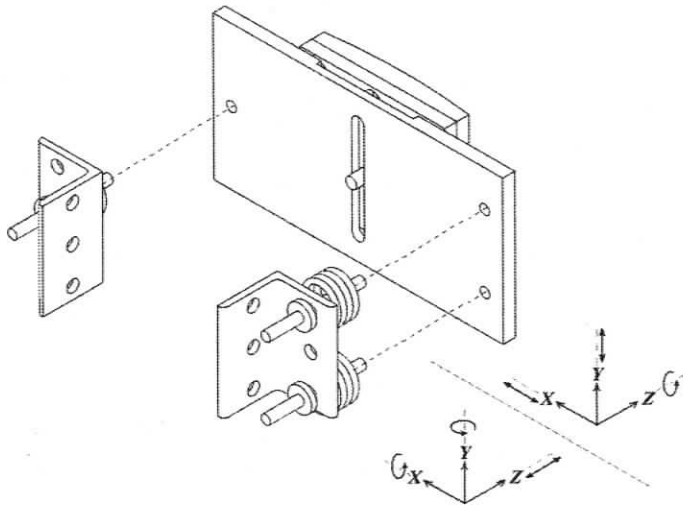

Figure 4-5: Two portions of the adjustable mount

The entire assembly is mounted to the inner surface of the main chamber wall. This ensures that the magnets in the field generator remained at room temperature throughout experiments.

4.1.4 Force Link

A mechanical link couples the force coil with the MARS clamp jaw. Requirements for the link include that it be stiff enough to transfer the force without deforming and that it be resistant to heat conduction. This second requirement is due to the temperature difference between the force coil and the MARS clamp jaw. The force coil remains at near room temperature while the clamp operated at 30 K. A 1.5 mm diameter G-10 rod is used to act as this link. G-10 is stiff and has an extremely low thermal conductivity. The G-10 is linked to the MARS clamp via a rigid clasp manufactured from copper sheet. The remaining end is attached to the force coil.

4.1.5 Link Lock

The second end on the G-10 rod is fixed to the force coil assembly. However, it could not be permanently fixed to the coil. In addition to low thermal conductivity, G-10 has very low thermal expansion properties. Despite this, it does contract slightly with a large drop in temperature such as the apparatus cooling from 297 K to 30K. In addition to the G-10 link, the coldhead, copper mounting plate and the clamp itself experience thermal

contraction during cool down. Because of this, and the importance of alignment between the force coil and field generator, the link between the clamp and coil must be free to move while the apparatus is cooling down. A clamping system capable of being activated from out side the chamber was needed which does not interfere with the force measurement.

The design of ths *link lock* mechanism underwent several design iterations before a suitable solution was found. The first design iteration used a solenoid with an iron plunger and is shown in Figure 4-6. The G-10 link passed through a small hole in an aluminum block. Another, intersecting hole, perpendicular to the first, accommodated the iron plunger. The plunger is suspended inside a solenoid which when energised would pull down on it. The plunger included a corresponding hole which when aligned with the first hole allowed the G-10 link to pass through the plunger. When left un-energized, the mass of the plunger is supported by the G-10 which is free to move in the hole restricted only by the friction due to the plunger weight. When energized, the plunger was pulled into the solenoid by the magnetic forces created. This additional force increased the friction on the link and held it firmly.

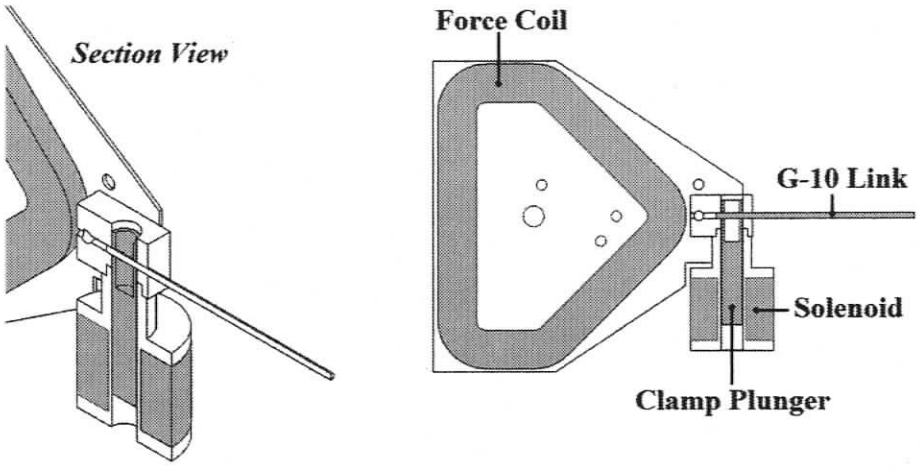

Figure 4-6: First design iteration of the *link lock* mechanism

This system performed adequately, however a significant problem arose upon using the link lock in a vacuum. In order to provide adequate clamping force, it was necessary to provide the solenoid coil with over 100 VDC of power. This generated over 15 W of heat

in the coil. It was found that in a vacuum environment, the solenoid temperature rapidly increased. Any lower power would result in link slippage. To counter this problem a second mechanism was devised. The new link lock utilized the same solenoid assembly but used mechanical advantage to increase the clamping force of the mechanism. This second design is shown in Figure 4-7. In this configuration the link lock used a copper lever to amplify the force subjected to the G-10 link by the solenoid. The solenoid was moved to a position under the force coil. When left un-energized, the mass of the lever pulled the clamp open and allowed the G-10 link to move freely in its guide hole. When energized, the plunger was pulled into the solenoid. This force was transferred to the copper lever which in turn exerted a force on the G-10 link. The copper lever included a knife edge at the point where it grasped the link and bit into the G-10, securing it firmly.

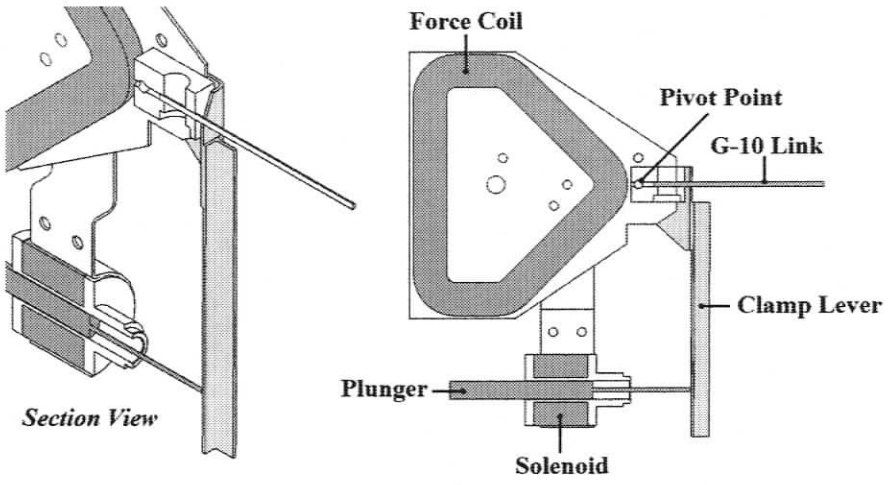

Figure 4-7: Second design iteration of the link lock mechanism

This configuration provided excellent clamping force while generating only 3W of heat. This effectively solved the temperature rise issue but created a new, unforeseen problem. Because of the solenoid's new location below the force coil it was in close proximity to the field generator. It was discovered that when the link lock mechanism was activated, electromagnetic forces pushed the entire force coil to the side. This displacement resulted in interference between the force coil and the field generator which yielded inaccurate force measurement results.

To solve this problem a third and final link lock mechanism was developed. This third iteration, shown in Figure 4-8, is an adaptation of the second design but employed a spring to apply force to the G-10 link. This configuration differed from the past two designs in that the un-energized state clamped the G-10 link while the energized state released it. When un-energized the spring exerted the necessary clamping force on the link. When energized the plunger was pulled into the solenoid which compressed the spring and allowed the G-10 link to move freely. Tests using this mechanism involved leaving the lock un-energized until the operating temperature was achieved. At this time, the solenoid was energized which released the link and allowed the displaced force coil to return to its proper alignment. The solenoid was then de-energized and the link was securely fastened to the force coil, ready for experiments.

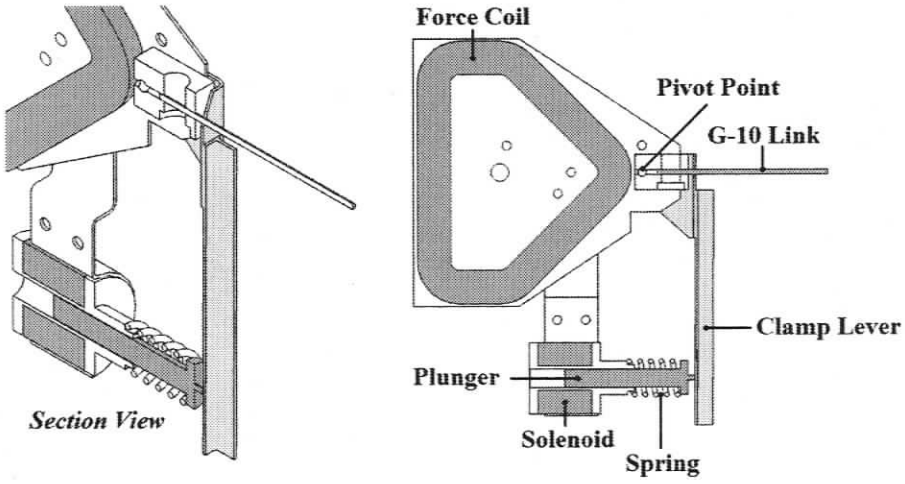

Figure 4-8: Final design of the link lock mechanism

Because it was only necessary to activate the link lock for a short period of time, it was possible to run the solenoid at a higher current without risking overheating. This allowed for a stronger spring to be used which allowed for greater clamping force than the second iteration was capable of exerting.

4.1.6 Complete Assembly

The final component for the force actuator is a support structure for the force coil. This structure supports the weight of the force coil assembly while allowing it to freely move in the Z direction. It is required that there be a minimum of mechanical resistance to motion of the force coil this direction as any friction in the support structure would affect the accuracy of the force measurement. To minimize the amount of friction a pendulum support was used. A rigid structure was built above the field generator from which the force coil is supported by thin wires. These wires were adjusted to position the coil both vertically and horizontally within the two poles of the field generator.

The force exerted by a pendulum due to a small displacement from equilibrium was given earlier in equation (2.16). Since the displacement of the force coil during operation is theoretically zero, the force due to this displacement is neglected.

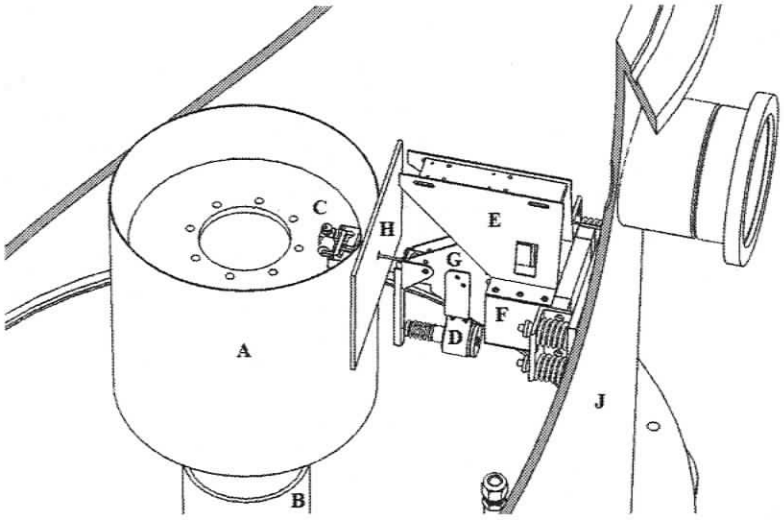

A Heat shield
B Cold-head
C Clamp assembly
D Link lock assembly
E Force coil support structure concept
F Field generator
G Force coil
H Magnetism shield
J Cryostat

Figure 4-9: Complete apparatus in cryostat

Once all designs were finalized, the complete apparatus was assembled and adjustments were made to ensure proper interaction between each component. Figure 4-9 shows the complete apparatus as it is installed inside the cryo-stat.

4.2 Calibration and Accuracy

Before the force measurement system could be installed in the cryo-stat, the force coil needed to be calibrated. To do this, a calibration apparatus was constructed utilizing the field generator and force coil arranged so that the force generated could be applied to a finely calibrated weigh scale. The scale used was a *Mettler PM2500* and had a resolution of 1 mg which was adequate for the calibration of the force coil. It was assumed that the force of gravity is 9.81 N/kg.

Calibration experiments focused on collecting two sets of data. First the effect of misalignment of the coil inside the field generator and, second, the relation between force generated and coil current. In order to collect this data, it was necessary that the calibration apparatus allow for adjustment of the coil's position inside the field generator so that it could be displaced by a known distance. An aluminum beam was placed over the scale supported on both ends by height adjustable tables. The field generator was suspended from this beam using a similar three bolt adjustment system to the final mounting design described earlier. This allowed the field generator to be levelled for the calibration. The force coil was mounted on a short stand which held it level. The force coil and its stand were placed on the scale such that the coil was correctly aligned inside the field generator. The entire apparatus is shown in Figure 4-10

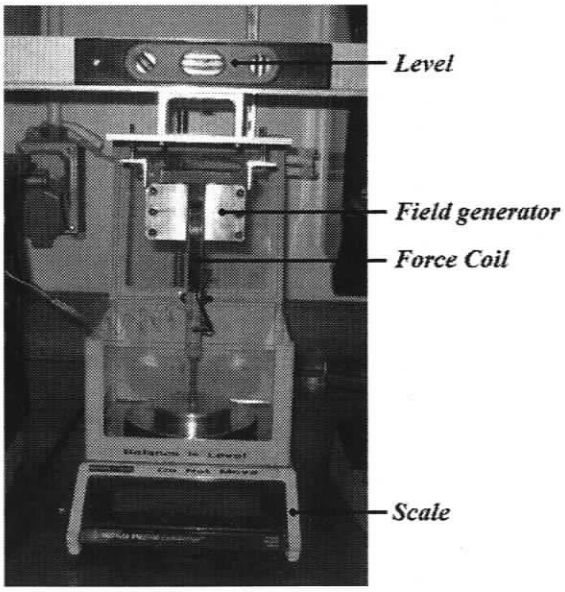

Figure 4-10: Calibration apparatus

In order to ensure repeatable setup of all calibration experiments, both the field generator and the force coil were scored with fine alignment markings. When these markings are aligned, the force coil is centered in the depth of the field generator gap as shown in Figure 4-11. This point was chosen as a base position from which all calibration measurements would be referenced and is defined as zero displacement for the following calibration experiments.

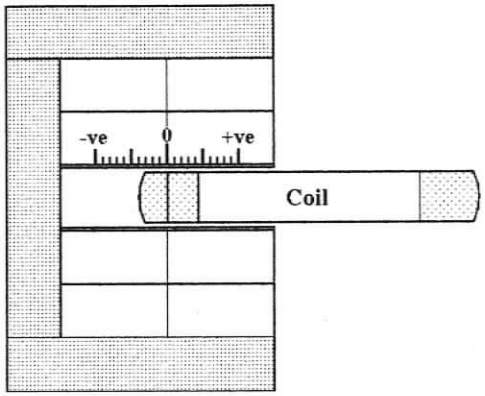

Figure 4-11: Force coil alignment inside the field generator

4.2.1 Calibration Method and Results

Calibration experiments started with determining the effect of offsetting the coil from the base position shown in Figure 4-11. The coil was energized with the maximum current of 20 mA. This current could be switched on and off easily using the DAQ software. The calibration began with setting the field generator height to the base position. The coil was energized and the scale was allowed to settle on a value. After the value was recorded, the force coil was deactivated and the field generator was displaced by an incremental distance. This procedure was repeated for a range of displacements from -15 mm to +15 mm from the base position in increments of 1 mm.

The results of the offset experiments are shown in Figure 4-12. The base point described above was set at position equal to zero. The positive scale indicates when the force coil was moved out of the field generator and the positive scale indicates when the coil was positioned further into the generator gap. This sign convention is illustrated in Figure 4-11 and corresponds to the z-axis defined in Figure 4-4.

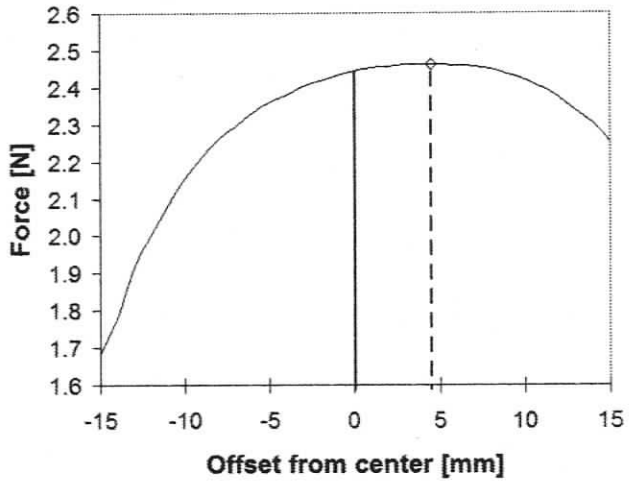

Figure 4-12: Force vs. offset from base point

It can be seen that the maximum force is not achieved at the base point alignment. The peak force actually occurred when the force coil was between 4 and 5mm out of the field generator. This point is indicated in Figure 4-12. This behaviour is supported by the FEA model of the field generator. When the magnetic flux density is plotted on the same line at the center of the field generator a similar curve was produced. This curve is shown in Figure 4-13. It can be that the peak field occurs approximately at positive 4-5 mm, coinciding with the calibration data.

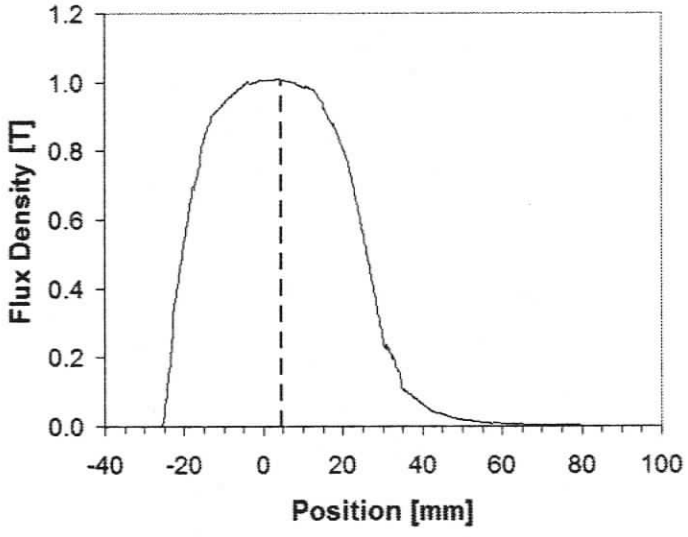

Figure 4-13: Flux density in field generator along z-axis

This information was used to set the position at which the coil was calibrated and used in the final configuration. A positive displacement from the base point of 5 mm offered both a higher available force and a more stable operating position. If the assembly were used with the coil set at the base point position, a misalignment of 1 mm would result in a an error of 0.38% or -0.49% depending on the direction of the misalignment. This is evident in the positive slope of the curve at this point in Figure 4-12. In contrast, the slope at the chosen operating position of positive 5 mm in the figure is near zero. If the assembly were used this position, a misalignment of 1 mm would result in an error of -0.03% or -0.08%.

Once the offset experiments were completed and the optimal position was determined, data was collected to find a relation between coil current and the force produced. The coil current was varied from 0 to 20 mA in 1.0 mA increments. The results are tabulated and several calibration runs are averaged to gain the plot shown in Figure 4-14.

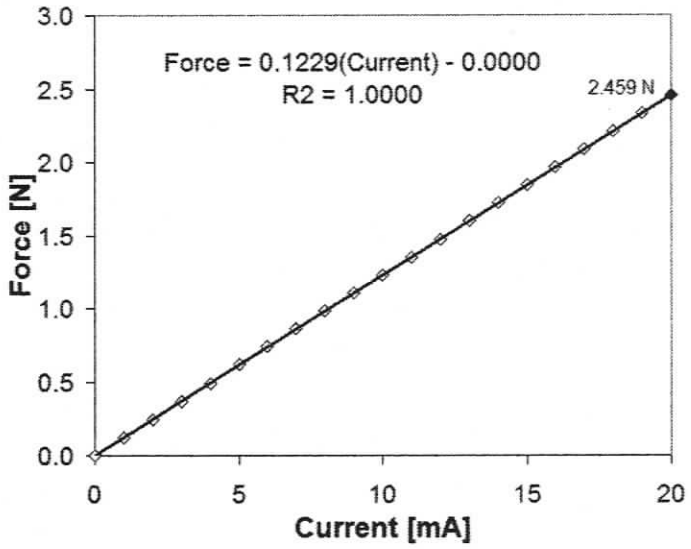

Figure 4-14: Force vs. coil current gained from average of several calibration runs

These results show that the relation is linear. The equation shown in the figure is that for a linear trend line which approximates the data. This experimental equation was used to calculate a theoretical force which was compared to the collected data. It was found that the maximum error between the calculated and averaged measured force is 0.12%

absolute or 0.0011% of full scale. This shows that the relation between the coil current and force can be accurately characterized as linear and approximated by the trend line equation (4.1).

$$F = 0.1229 I_{FC} \tag{4.1}$$

The repeatability of the force was also determined from the calibration data. As stated, the calibration was performed several times and the average data used to find equation (4.1). When all calibration runs were individually compared to this equation, the maximum error was found to be 0.643% absolute or 0.635% of full scale. This low error shows that the calibration is repeatable.

4.3 Test Procedure and Instrumentation

The instrumentation system developed for the MARS experiments is as important as the individual components which make up the test apparatus. The instrumentation system was developed around *National Instruments, LabVIEW* software which collected data as well as controlled the various components.

4.3.1 Experimental Procedure

The basic function of the test apparatus involved slowly increasing the force on one of the MARS clamp jaws until it fails. This simple task was achieved by slowly increasing the current in the force coil while monitoring the clamp jaws to identify the point at which they opened. At this time the maximum force was recorded and force coil current was returned to zero. This procedure was repeated several times in order to check for consistency of results.

The following is a step by step representation of a complete room temperature experiment which is intended to generate a curve relating clamping force to clamp coil current I_{CC}.

1) Clamp coil current set to 0 mA
2) Current in force coil slowly ramped from 0 mA until clamp jaws open
3) Maximum force coil current recorded and output returned to 0 mA
4) Steps 2 and 3 repeated n times
5) Clamp coil current incremented by ΔI_{CC}
6) Steps 2, 3, 4 and 5 repeated until a specified maximum clamp coil current is reached

Low temperature experiments differ from room temperature test in that steps 5 and 6 were not performed automatically. Because of the limited time for running experiments during system warm up, steps 2-5 could only be performed once, or possibly twice, before the cooling system had to be restarted to return the system to its starting temperature. Therefore I_{CC} was increased manually and only one or two data points could be collected at a time.

4.3.2 Instrumentation Design

The instrumentation system wad developed around *National Instruments* DAQ hardware coupled with *National instruments LabVIEW* software. The hardware collected input signals and delivers control signals via wires routed through feedthroughs into the chamber. Each pair of wires performed a specific task and was controlled or monitored by individual channels in the DAQ system. A list of each channel and its function is given in Table 4-2.

Table 4-2: Data acquisition channels

Input

Channel	Description	Range
0	Clamp Open Test Output	0 – 10 V
27	Clamp Voltage	0 – 10 V
Serial	Temperature	-

Output

Channel	Description	Range
2, 4	Light Power	0 – 20 mA
0	Force Coil Power	0 – 20 mA
1	Clamp Open Test Power	0 – 0.1 mA
3	Clamp Power	0 – 10 V

The input channels were used to control the clamp power, record temperature as well as to test for the clamp jaw's open status. The output channels were used to test for the clamp jaw's open status as well as control the clamp coil current, the force coil power and two LED lights which illuminated to interior of the chamber.

The *Clamp Voltage* measured the voltage drop across the clamp coil. This data was used along with the manually measured clamp coil resistance to calculate the clamp coil current. This was used in conjunction with the *Clamp Power* output channel which sent a DC voltage signal to an amplifier circuit which in turn delivered power to the clamp coil. A simple proportional control algorithm was used which adjusts the *Clamp Power* based on the value of the *Clamp Voltage* signal.

The two channels, *Clamp Open Test Power* (COTP) and *Clamp Open Test Input* (COTI) were used to test for the status of the clamp jaws. This test was conducted by attaching a wire to each clamp jaw. Through the COTP channel, a small current of 0.09 mA was passed through these wires and through the jaws. COTI monitored the voltage drop across a 100 kΩ resistor which was wired in series with the clamp jaws. In this circuit the clamp jaws acted as a switch as shown in Figure 4-15. When the jaws were closed, the circuit was complete and the current passed through the resistor. In this state, COTI would see a ~9 V voltage drop across the resistor. Upon opening of the clamp jaws, the current through the circuit, and thus the voltage across the resistor, both dropped to zero. The software was programmed to watch for this and characterise it as a "clamp open" event.

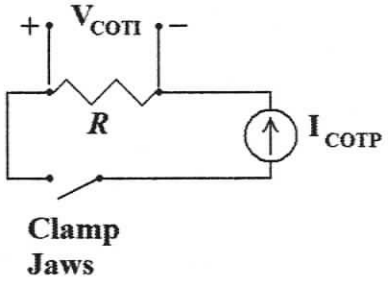

Figure 4-15: Simplified circuit diagram of clamp open test

The *LabVIEW* software was programmed to perform the experimental procedure as outlined in section 4.3.1. A small sub-program was created which rapidly cycled itself until the clamp jaw opened. During each cycle, the force coil current was incremented by a constant amount which was input by the user. The status of the clamp open test circuit is queried after every incremental force coil current increase. Once the clamp jaws separated, the sub-program stopped and output the maximum force coil current. The output maximum current was manipulated by the main program to convert the force coil current to a force value using equation (4.1) and was output to a text file. During operation, additional data such as temperature, date and time and ramp rate were collected and output to a text file which was formatted to allow easy import into a spreadsheet for analysis.

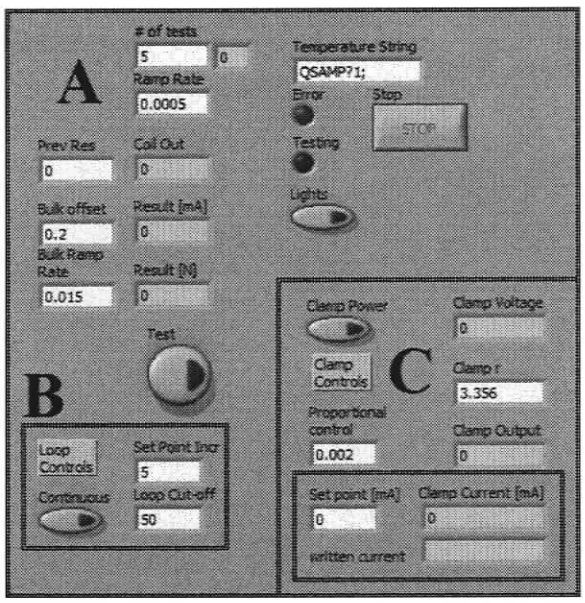

Figure 4-16: Front panel of DAQ program

Figure 4-16 shows the front panel of the DAQ program and is divided into three main sections. The section labelled "A" deals with the overall experiment as well as the results. The field "# of tests" was used to set the value of *n* in step 4 of the procedure. This value controlled how many experiments are conducted for each data point on the performance curves. The "ramp rate" field set the amount that the current was incremented for each cycle of the sub-program. "Previous Result", "Bulk Offset" and "Bulk Ramp Rate" were all used to control the bulk ramp rate of the force coil. In order to reduce experiment

time, the ramp rate was increased to the "Bulk Ramp Rate" value and the experiment was run until the force coil current reached a value which was lower than the previous maximum current recorded. The "Bulk Offset" controlled how much lower that value should be. Once the value was reached the ramp rate was reduced to the value of "ramp rate" and the experiment continued until the clamp opened. This provided quick experiments which still yielded accurate results.

The section labelled "B" in the figure was used to control the automatic looping of the experiment. "Set Point Incr." dictated the amount in mA that the clamp coil current was increased between data points. "Loop Cut-off" set the maximum clamp coil current that would be tested, while the button labelled "Continuous" was used to set whether the program would automatically produce an entire performance curve or just a single data point.

The section labelled "C" was used to control and monitor the power delivered to the clamps. As mentioned, the program used a proportional control method to control the current through the clamp coil. The "Clamp r" field was used to set the resistance of the clamp coil which along with the value of the "Clamp Voltage" was used to calculate the current through the clamp. "Proportional control" set the value of the proportional constant in the controller.

Other buttons and indicators were used to monitor the status of the program as well as control the lights and start and stop the individual experiments. The values shown in each field represent the default settings which were used for the majority of experiments.

4.4 Summary

The design and construction of the first iteration of the apparatus has now been completed. The calibration of the apparatus has shown that it performs as expected and is ready for testing. The following chapter will discuss initial test results as well as refinements to the design which were deemed necessary after analysing those results.

Chapter 5 Testing and Design Refinement

5.1 Initial Test Results

The results from the first set of experiments were promising and can be seen in Figure 5-1. They show a near linear relation between clamping force and clamp current. However, the magnitude of the force produced is a close match to that which was predicted using the FEA model discussed in section 2.3. This was unexpected since the shutter material was included in the FEA model but not the experiments. The absence of the shutter material should have improved the clamps performance

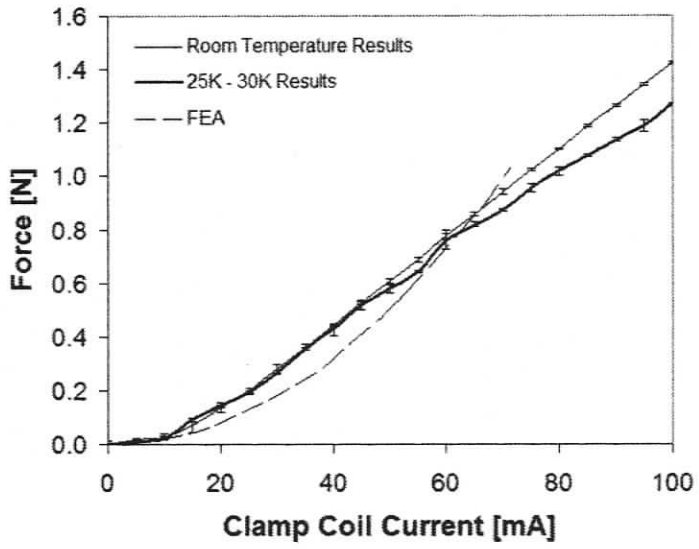

Figure 5-1: Initial results

The irregular nature of the cryogenic temperature curve is due to changes in the force coil current ramp rate. During the cryogenic experiment, it was noticed that the link lock solenoid was rapidly increasing in temperature. The first link lock design was in use during these experiments and, as described earlier, this design required significant power to secure the link which caused rapid temperature rise. In order to limit the temperature rise and prevent damage, the ramp rate for the cryogenic experiments was increased and the erratic results in Figure 5-1 were noticed. These results prompted the study of the effects of force coil ramp rate which is described in the following section.

5.2 Effects of Force Coil Current Ramp Rate

As mentioned, the rate at which the force coil current was increased affected the outcome of the experiments. A series of experiments were conducted which performed the same experiment repeatedly using different force coil ramp rates to better understand these effects and to determine the optimum ramp rate. A portion of the results from these experiments is shown in Figure 5-2.

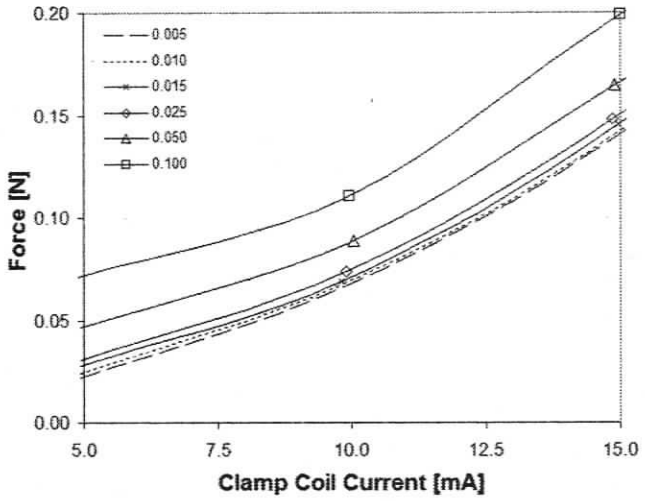

Figure 5-2: Results of force coil current ramp rate experiments

The figure shows six plots of the performance curve for a single clamp, each at the ramp rate shown in the legend. The units of the ramp rate are mA/cycle. Every time the sub-program described in section 4.3.1 was looped, the force coil current was increased by the amount shown. It can be seen that the results of each experiment differ by a significant amount. The results generated using a force coil ramp rate of 0.10 mA/cycle show a higher clamping force than those generated by a ramp rate of 0.050 mA/cycle. This was due to timing issues with the LabVIEW program. At higher ramp rates, the program could cycle past the breaking force before the clamp open test circuit could react to an open clamp event. Slower ramp rates reduce this error by minimising the amount that the program can overshot the coil current. There is a similar reduction found when the ramp rate is further decreased. It is observed that subsequent decreases of force coil ramp rate resulted in ever decreasing performance of the results and the curves converge to a minimum. When the ramp rate was reduced to 0.005 mA/cycle, it can be seen that

there is minimal change in the output vs. the previous ramp rate of 0.010 mA/cycle. It was decided that a force coil ramp rate of 0.005 mA/cycle would be sufficiently low enough to produce accurate measurements of the clamping force.

5.3 Result Verification

To verify the measurements produced by the test apparatus and to improve over-all confidence in the test apparatus, a measurement verification procedure was developed. This procedure involved supporting the clamp in a vertical configuration and using suspended mass to force the clamp jaws open. Great care was invested to ensure good confidence in the results of these experiments. The same DAQ system was used to power the clamp and watch for clamp jaw open status as was used in the main experiments. The experiment apparatus was removed from the chamber intact and oriented such that a weight could be suspended from the clamp jaw. This ensured that there was no alteration of the apparatus due to disassembly and reassembly.

The verification procedure was performed similar to the main experimental procedure and is outlined as follows.

1) Clamp coil current set to 0 mA
2) Mass is added to the weight until the clamp jaws opened
3) Weight is measured on a high accuracy scale and recorded
4) Clamp coil current incremented by ΔI_{CC}
5) Steps 2, 3, 4 repeated until a complete curve is obtained

Mass was increased in the form of zinc particles placed into a light weight plastic vessel suspended from the lower clamp jaw. The zinc particles varied in mass from 0.034 g - 0.092 g. and were added to the plastic vessel until the clamp jaw opened. A small number of particles were then removed and the clamp jaw was closed. The mass was re-suspended from the lower jaw and particles were carefully added one at a time until the clamp opened again. The suspended mass was then weighed on the same scale used during calibration of the force coil. These mass experiments were repeated several times to ensure repeatability and to increase confidence in their results. The process was extremely time consuming but produced results with a high level of confidence.

Results of the verification experiments are shown in Figure 5-3. The average mass verification curve shown is averaged from three curves generated using the above procedure and is shown with the individual curves. It can be seen that the error between each curve is small. The maximum error between the verification curve and the three curves is f 2.2%FS.

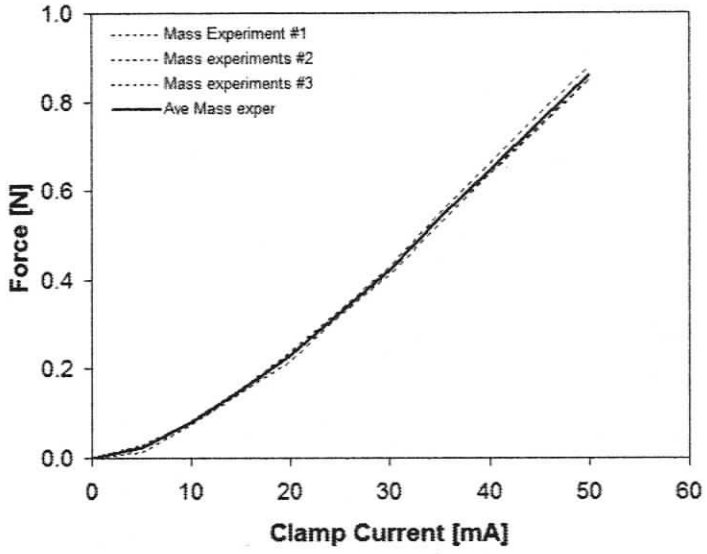

Figure 5-3: Results of verification experiments

With the verification curve as a reference, the test apparatus was returned to the cryostat and connected to the experimental apparatus. A series of experiments were then run to test the accuracy of the experimental apparatus. The results are shown in Figure 5-4. It can be seen that the experimental results are close to the verification curve. When the error between each curve and the reference curve is calculated the maximum error is found to be 5.4%FS or 0.05N and an average error of 2.0%FS or 0.017 N. The maximum error between the three experimental runs is found to be 0.022%FS or 0.020 N.

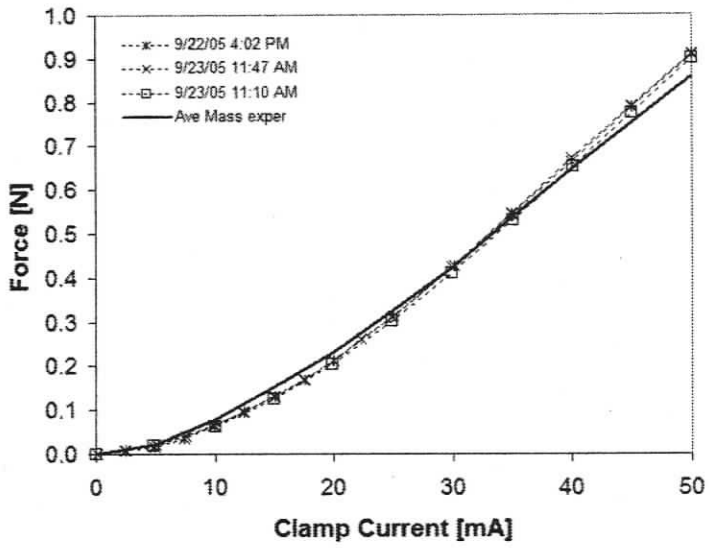

Figure 5-4: Comparison between verification curve and experimental results

5.4 Effects of Clamp Testing Assembly Adjustments

A series of experiments were performed in order to determine if the clamps could produce repeatable results despite undergoing disassembly and re-assembly. The verification curve described in section 5.3 was used as a reference for these experiments. This was chosen because it represents the performance of the clamp in its initial assembled state. To begin the experiment the clamp assembly was disassembled. Great care was then taken to ensure that it was reassembled with the same alignment. The clamp was then reinstalled in the chamber and a new curve was generated. The results of this experiment are shown in Figure 5-5

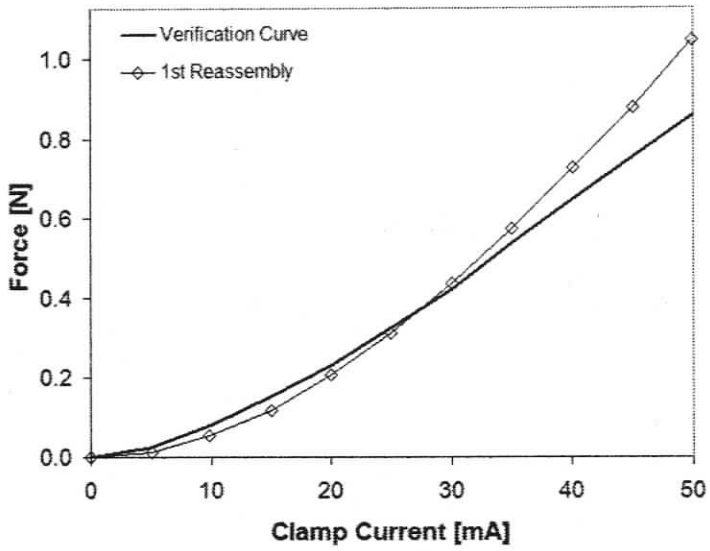

Figure 5-5: Results of initial clamp repeatability experiments

It was found that the performance of the clamp differed from the initial performance. To verify that this was not a problem with the test apparatus, the clamp and mounting plate were again removed from the chamber and setup for further mass experiments. The results of this experiment are shown in Figure 5-6.

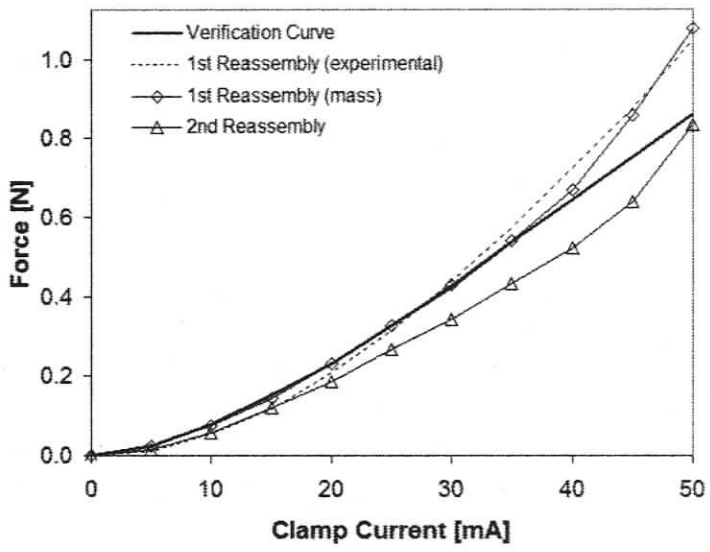

Figure 5-6: Mass verification of clamp performance after reassembly

The mass verification curve closely mimicked the test apparatus results for the reassembled clamp which confirmed that the clamp performance had changed. To further

explore the problem, the clamp was disassembled and reassembled a second time. Again, great care was taken to ensure proper alignment between the clamp jaws during assembly. The results of the second experiment are also shown in Figure 5-6. The third performance curve did not match the reference curve or the curve from the first reassembly.

It was theorized that the link design is the cause of these inconsistent results. All of the previous experiments used the original rigid copper clasp to hold the jaw. The copper is formed to grasp the clamp bar securely but it was found that the design was too wide and caused uncertainty as to the exact location along the length of the jaw that the force was applied. As well, it was possible that the clasp is introducing undesired moments into the system.

To counter this problem, a second force link design was developed. This clasp was manufactured from thin copper wire. The much narrower design allowed for greater certainty of the application point of the force. This second force link was installed with the apparatus still in the mass experiment configuration. The clamp was left unperturbed from its second reassembly and the new wire link was placed such that the applied load was centered between the two clamp legs. The results of this experiment are shown in Figure 5-7.

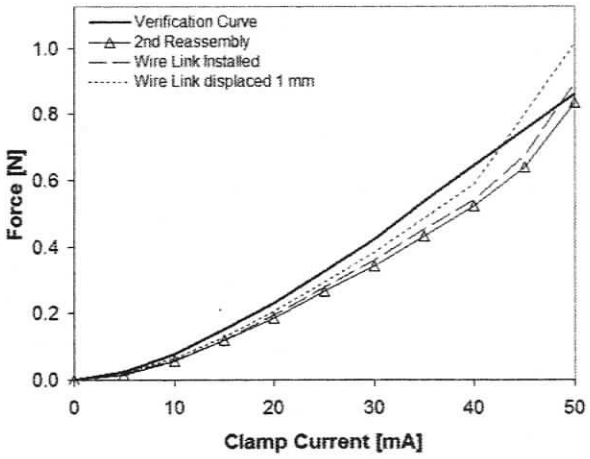

Figure 5-7: Results of new wire-based force link design

The results of the wire link are close to those of the initial link design. However, when the link is purposefully displaced such that the applied load was 1 mm closer to the outer clamp leg, the results are significantly affected and are closer to the results of the first reassembly experiment. This result shows that placement of the force link on the clamp jaw is of great importance.

Further experiments were conducted with the new force link. Each time the clamp assembly was disassembled and reassembled or even slightly perturbed, the test results varied dramatically. Every effort to provide consistent assembly conditions failed to produce repeatable results. It was decided that a new method of supporting the clamp jaws was needed in order to rule out jaw alignment as a source of error.

5.4.1 Clamp Jaw Support Assembly

The original clamp design employed flexures to support the lower jaw. This system produced uncertainty of the quality of clamp jaw alignment. Despite the use of micrometers and careful adjustment of the assembly, it was found that jaw alignment could not be reproduced after disassembly of the apparatus. This was a concern since it is desired to compare several clamps of different shapes and materials. If a consistent performance could not be assured, there could be no confidence in the results of the clamp comparison experiments. The initial clamp assembly using the flexures is shown in Figure 5-8. These flexures allowed the clamp jaw to open and close freely. However, they held the clamp bars rigidly and produced small misalignments between the two jaws if not perfectly mounted.

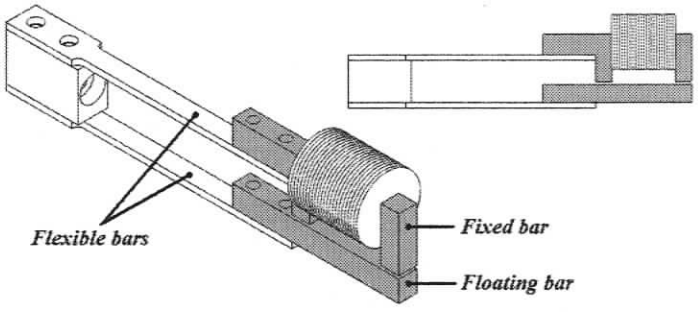

Figure 5-8: Initial clamp design assembly

The new design employed an aluminum cradle to support the weight of the lower clamp jaw while allowing it to move in all directions. This allowed the lower jaw to orient itself such that it could align to the statically mounted main clamp jaw. The force which would pull the lower jaw into the main jaw was the electromagnetic attraction between the jaws themselves. Also, two small springs provided a small amount of pressure in the direction of the main jaw. The springs were included to ensure that the jaw would return to its original, closed position after each test. The new clamp support assembly is shown in Figure 5-9. The clamp bars themselves are shown shaded while the components of the assembly are indicated.

A Clamp cradle
B Clamp coil
C Clamp mounting block
D Cernox temperature sensor
E Force link gap
F Springs

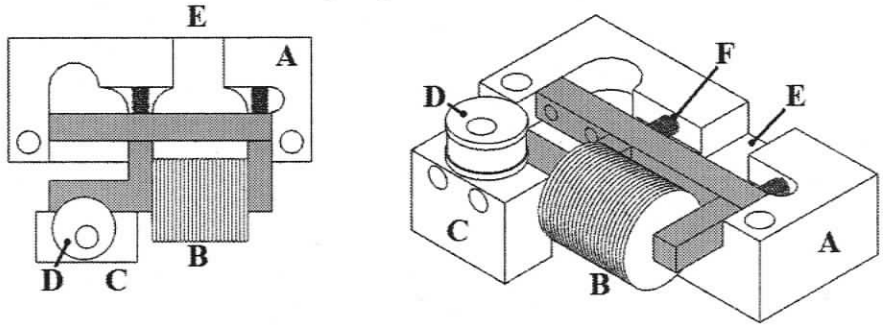

Figure 5-9: Final clamp jaw support assembly

The new assembly is installed in the chamber test apparatus and a set of preliminary experiments were performed. The experiments were conducted using the same procedure as before and using the new wire based force link. The results of these experiments are shown in Figure 5-10. The original mass experiment verification curve is included for reference.

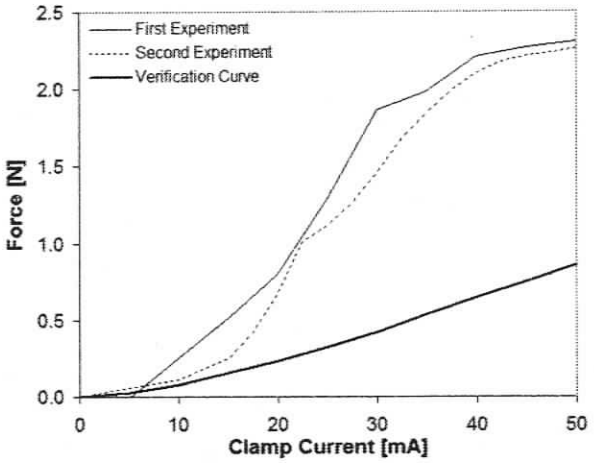

Figure 5-10: Results of new clamp support assembly

The initial results show two important features. First, the curves show a clamp performance which significantly exceeds the previous results shown by the verification curve. This result supports the assertion that the original clamp support structure was interfering with the clamp performance. The second feature of interest is the erratic nature of each curve while all previous experiments yielded smooth curves. It was discovered through close examination of the clamp assembly that the wire based force link was twisting the floating clamp bar. Under the original configuration, the flexure structure was rigid enough to counteract this twisting. However, the new free floating bar can not, which results in the inconsistent performance shown.

5.4.2 Second Force Link Redesign

In order to eliminate undesired moments from the system a third force link was developed. The second force link design proved to be problematic in that it produced a moment about an axis running along the length of the bar. It is theorized that this twisting load produced premature failure of the clamp which in turn produced the erratic results shown in Figure 5-10. The new design used a short length of nylon string looped around the clamp jaw in conjunction with a hook fashioned from copper wire. This design provided certainty of the load application point and minimised all undesired moments. Figure 5-11 shows all three force link designs. The original link is shown in the background while the second, wire-based design is in the middle. The final design is shown in the foreground. A MARS clamp is included for size reference.

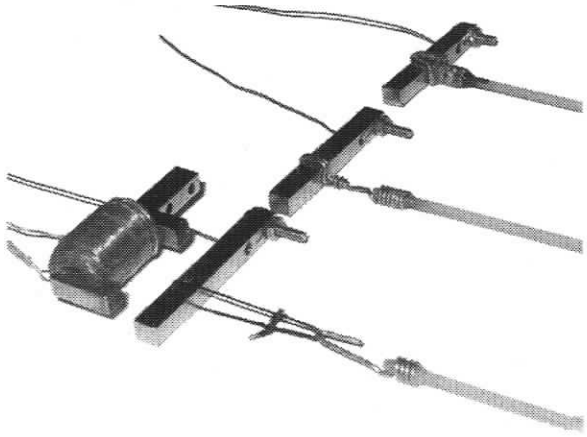

Figure 5-11 Three configurations of the force link

The new force link was installed in the apparatus and a series of tests were performed. The results of which are shown in Figure 5-12. Between each experiment the assembly was perturbed to check for repeatability. This involved removing the lower clamp jaw and reinstalling it. Despite this, it can be seen that all three experiments produced similar curves. However, the three curves did not follow the path of the original mass verification experiments. It was decided to repeat the verification experiments without the interference of any clamp support structure. The mass experiment was setup for a third time using the same procedure as past verification experiments. However, for this experiment, all clamp support structures were removed and only the electromagnetic attraction between the clamp jaws was used to hold the lower clamp bar in place. This configuration ensured that there was no interference between the jaws and they were allowed to fully close. The resulting curve is shown in the figure and it can be seen that it closely matches the three experimental runs for the initial portion of the curve. However, the two curves diverge away from the verification after I_{CC} exceeded 20 mA.

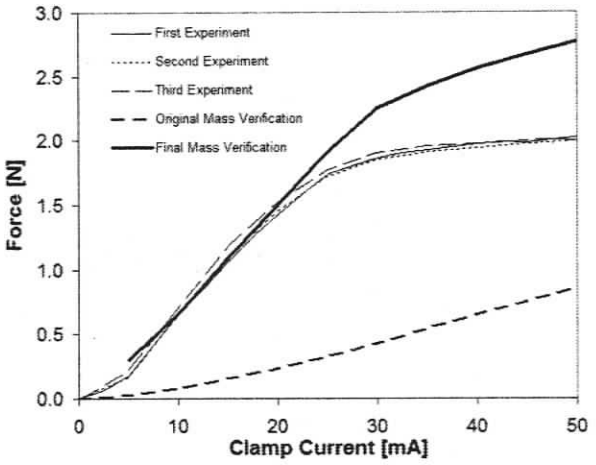

Figure 5-12: Results after third force link was installed

5.5 Effects of Clamp Current Polarity

With the new clamp support assembly and third force link installed, results from the test apparatus were consistent. However, after a large number of experiments were conducted a new problem in the results became apparent. The performance curves were relatively repeatable but two distinct sets of curves developed as seen in Figure 5-13. The "group 1" curves closely follow the verification curve until they reach the maximum force which the apparatus could exert. This limit is shown in the figure as a finely dashed horizontal line. The "group 2" curves follow the verification curve up to a clamp coil current of approximately 20 mA but then deviate and appear to reach saturation at a lower force.

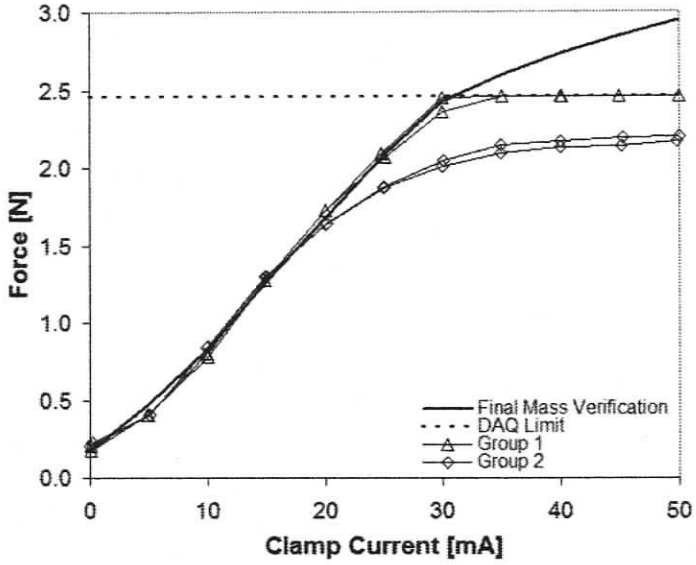

Figure 5-13: Final test configuration results showing two groups of performance curves

Several experiments were performed in an effort to determine the cause of this problem. Eventually it was discovered that the direction in which the clamp coil current was driven dictated which group the results would fall under. Aside from mass verification experiments, all previous experiments were conducted with the coil current connected in a random fashion. Each time the apparatus was installed, the clamp coil was connected without consideration of the current direction. This was done because there was no reason to expect that the current direction would affect their performance.

Originally it was theorized that other lab equipment including, a 5 T magnet, was affecting the results of the experiments. However, when this equipment was deactivated, the problem persisted. Further investigations showed that the cause of the problem was stray magnetic field from the field generator. FEA models showed a small amount of magnetic flux was reaching the clamp assembly and passing through the high permeability clamp bars. When the field in the clamp was aligned with this stray field, the clamps experienced saturation at a lower clamp coil current than when the fields were anti-aligned. The model showed that the addition of a steel plate between the field generator and the clamp assembly would reduce the stray field strength by 97%.

Therefore a magnetic shield was constructed from 6.4 mm thick mild steel measuring 15 cm by 10 cm. The shield was bolted to the copper radiation shield between the clamp and the field generator as shown in Figure 4-9. A small hole was included in the center of the plate to allow the force link to pass through. A series of experiments were conducted with the new shield installed in the chamber. It was found that the addition of the magnetic shield removed all dependence on the clamp coil current direction.

5.6 Summary

In this chapter, problems with the test apparatus were identified and remedied. Problems ranged from unforeseen magnetic interactions to alignment issues between the clamp jaws. Despite these problems, it has been shown that the apparatus performs well and is capable of providing accurate measurements of the clamping performance of the MARS clamps. The following chapter will explore the results of the first experiments which focus on the clamps themselves as opposed to the development of the test apparatus.

Chapter 6 Results and Discussion

The development of this test apparatus was driven from the need to optimise the small electromagnetic clamps to be used on the MARS. These clamps are fundamental to the operation of the proposed MARS device and must be able to deliver enough clamping force to securely hold the shutters during displacement. In order to optimise these clamps, it was necessary to have an accurate method of measuring their clamping force. All of the experiments discussed thus far were performed in order to validate and refine the original design of the clamping force testing apparatus. The following experiments focus on the initial test results of the clamps themselves.

In order for the test apparatus to be a viable tool in the optimisation of the clamps, it must be able to provide accurate force measurements with a high level of confidence in the results. Many of the tests performed were focused of improving the repeatability of the experiments. It was found that small perturbations of the test clamp heavily affected the results of the experiments. However, when the clamp was left undisturbed, the experimental results were consistent. This indicated that the apparatus is capable of consistently measuring the clamping force of the test clamp and the source of results inconsistency is the clamps themselves. The clamps were found to be extremely sensitive to jaw alignment.

Using the original flexure system to support the clamp jaws, a series of experiments were conducted which tested the same clamp several times. Between each test the clamp was removed and adjusted. The results showed a 50 mA clamping force which varied from 0.65 N to 2.31 N. This is a 258% difference between the lowest and highest force. Great effort was invested to improve the repeatability of the experiments by using micrometers and shims to align the jaws in the flexure mounts. However, no improvement was noticed.

When the new clamp support assembly was used, the repeatability of the experiments greatly improved. A series of nine experiments were performed. The 50 mA force varied

from 2.00 N to 2.31 N which is a difference of 15.6%. Adjustments to the new jaw support assembly as well as the addition of a magnetism shield to block stay magnetic field from the field generator from reaching the clamp helped to improve the repeatability of the experiments. However, a 50 mA clamping force could not be measured because the test apparatus reached its maximum output before the clamps failed at that coil current. Despite this, the results showed an improved level of repeatability with a 25 mA clamping force which varied by only 9.8%.

6.1 Addition of Stainless Steel Shutter

With the apparatus design refined such that results were consistent, work focused on collecting experimental results of the clamp performance. All previous experiments were conducted with the clamp jaws fully closed. This configuration increased the clamping force of the clamps above what the test apparatus could measure. However, the MARS clamps are required to grasp a thin shutter which will be inserted between the jaws spacing them apart. During the FEA modeling, a 0.05 mm wide gap was used which corresponds to the thickness of the stainless steel shutters used in the MARS prototype. The maximum force of 1.33 N found using the FEA model is well within the test apparatus's range of 2.46 N.

A small strip of the stainless steel shutter was inserted between the two clamp jaws in the test apparatus which spaced the jaws the correct distance apart. A number of experiments were performed, the results of which are shown in Figure 6-1. The vertical dashed line indicates the 50 mA point which is the intended operating current of the clamp. [2] The performance curve produced by the FEA model is included and the force it predicted at 50 mA is indicated.

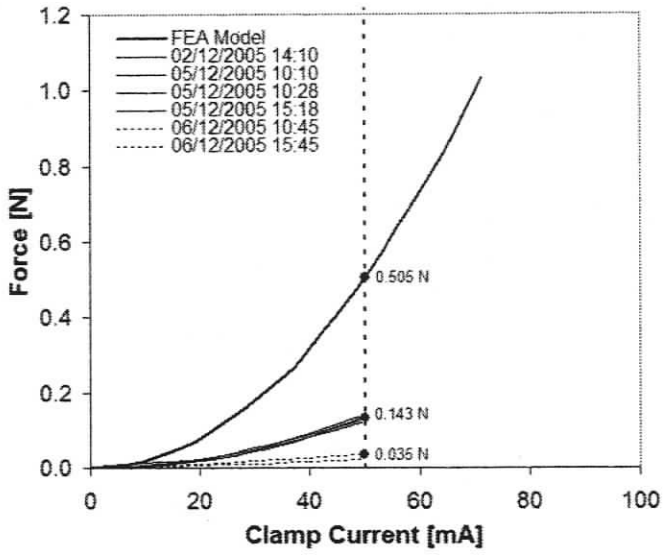

Figure 6-1: Initial results of clamp tests when shutter material is added

It can be seen that the addition of the shutter material reduced the performance of the clamps considerably. However, the amount of performance reduction is much greater than expected. The first four curves generated yielded a clamping force of approximately 0.143 N at 50 mA which is 72% lower than the expected force found using the FEA model. When the lower clamp jaw is removed and replaced, the fifth and six curves are produced. These curves show a clamping force of approximately 0.035 N which is 93% lower than what is predicted by the FEA model. Although significant work was invested in increasing the repeatability of the test apparatus, these results how that the addition of the shutter material produced additional inconsistencies. A series of repeatability experiments were performed on the clamps with the shutter material in place.

6.2 Further Repeatability Tests

The previous experiments showed that repeatability is still an issue. To test repeatability a number of experiments were conducted which involved the removal and reinstallation of the lower clamp jaw. This was intended to mimic the effects of changing between clamps during clamp design comparison experiments. The results are shown in Figure 6-2. It can be seen that there are significant problems with the repeatability of these experiments. Experiments #2 and #3 were run past the intended clamp coil current to determine clamp

behaviour at higher coil currents. It can be seen that experiment #3 reaches saturation at approximately 95 mA.

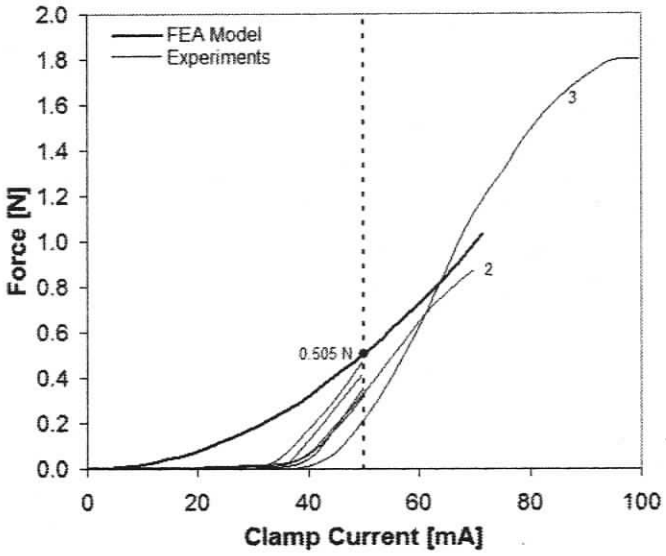

Figure 6-2: Results of repeatability experiments with shutter material installed

Keeping the shutter material flat and straight between the two jaws proved extremely difficult. If the shutter were to bend it would complete the circuit between the upper and lower jaw and mislead the control system into believing the clamp were still closed. This problem is manifested by the flat portion of the performance curves noticed in Figure 6-2. This region of zero clamping force was caused by the shutter material bridging the gap between the clamp jaws after they failed. The output remained constant until the force required to pull the clamp jaws apart exceeded the force required to pull the jaws far enough apart to break the circuit caused by the bent shutter material. The force is zero in this region because the initial measurement taken at a clamp coil current of 0 mA was subtracted from all following values to account for preload in the springs.

A second set of repeatability experiments involved replacing the lower jaw of the clamp assembly. Although replacing the entire clamp would be a more definitive test of clamp comparison accuracy, it was decided to undertake the simpler task of replacing only the lower jaw while allowing the upper jaw and coil to remain fixed in place in the test apparatus. Each of the three lower jaws tested were identical in size and material make

up. For these experiments, the shutter material was removed as it was hoped that the previous results found during testing and development could be repeated. However, when the new set of repeatability experiments were conducted, it was found that none of the three lower jaws tested matched the original results including the original jaw itself. This can be observed in the results shown in Figure 6-3.

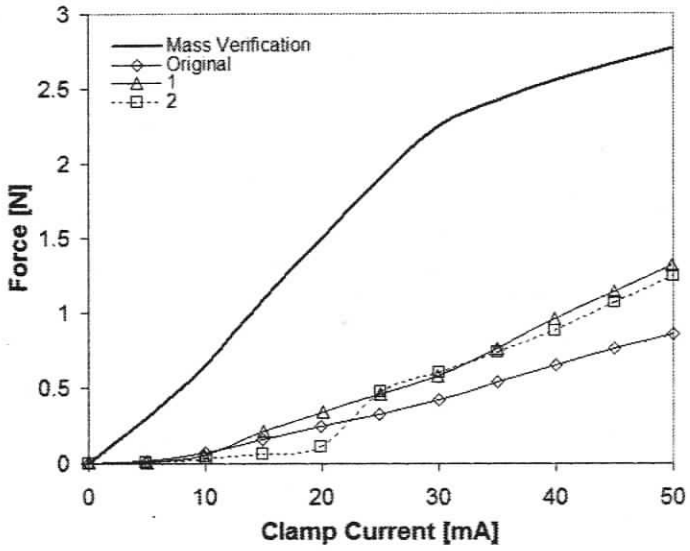

Figure 6-3: Results of clamp jaw replacement experiments

6.3 Validation of Test Apparatus

Experiments conducted during the development of the test apparatus showed that it is capable of producing accurate and repeatable results. Calibration experiments showed that the force coil and field generator could be modeled using a linear equation with a maximum error of 0.0011% FS. The maximum repeatability error was found to be 0.635%FS. The effect of the alignment between the two components was also examined. It was found that a misalignment of ± 1 mm would result in a maximum error of 0.08%. This level of misalignment would be clearly visible to the operator and could be corrected. These results showed that the basic concept of the design could be used to exert a predictable force with high accuracy.

The verification of the measurement system was conducted by using a simple mass system to determine the clamping force of one clamp. The verification process involved

using suspended mass to force the clamp jaws open. When the clamp was returned to the test apparatus, it was found that it could duplicate the results of the mass verification with a maximum error of 5.4%FS or 0.05N.

Upon completion of the entire test apparatus, its repeatability was again verified. A number of experiments were conducted without disturbing the clamp between runs. It was found that the maximum error between experimental runs was 0.022%FS or 0.020 N. However, this repeatability was limited to cases where the clamp was left undisturbed between experiment runs. If the clamp was perturbed, the results varied significantly. Extensive work was invested to solve this problem in order to allow clamps to be removed and replaced with confidence that the results would not be affected. This work involved the design and construction of a new system of supporting the clamp jaws in the chamber. The new system allowed the lower clamp jaw to float freely whereas the original flexure based system held the jaw rigid such that alignment issues would arise. These alignment issues resulted in repeatability errors as high as 258%. The results of the new system showed that repeatability is improved significantly. The late addition of a magnetism shield solved an issue with stay field from the field generator affecting the clamp performance. Coupled with this shield, as well as improvement of the force link, the new clamp support system helped reduce the repeatability error to 9.8%.

The mass verification procedure was repeated with the new apparatus. This time, the verification experiment was conducted with no clamp support system. The lower jaw was held to the upper clamp jaw solely by the electromagnetic force between them. This ensured there was no outside interference between the two jaws and is viewed produce to be the true performance of the clamp. It was found that the experimental results of the new apparatus fit the verification curve with a maximum error of 2.23%FS up until the curve exceeded the measurement range of the test apparatus.

6.4 Clamp Design Analysis

Alignment issues with the clamp jaws themselves prevented any meaningful cryogenic testing being performed. Only one performance curve was generated at cryogenic temperatures. This experiment was intended to test if the assembly could function at the desired temperature and was performed early in the testing regiment before the apparatus was refined. The results of this experiment showed that the test apparatus performed as designed at cryogenic temperatures and complete vacuum.

The main issue with the clamp design was the inability to achieve consistent performance. It was found that small errors in alignment would result in vastly different performance from the clamp. Despite careful preparation of test clamps, experiment repeatability proved to be a difficult goal to attain. This problem reduced the ability of the test apparatus to characterise the clamps performance with any confidence. Since one goal of this project is to determine which clamp design and material would provide the best performance it is necessary to test several clamps. However, since removing or adjusting the clamps caused so much variability in results, no confidence can be drawn from experimental results if the clamps are disturbed in any way.

Although a new system of clamp jaws support was devised to increase the repeatability of experiments, the MARS device requires the use of the original, flexure based, jaw support. This system proved to be the most problematic. It allowed for minimal adjustment of the clamp alignment which resulted in poor repeatability. Should this system be improved to allow for confident alignment of clamp jaws, the repeatability problem may be alleviated.

The optimisation of the MARS clamps has the primary goal of reducing the clamps size and weight. This would involve designing a clamp which can provide adequate clamping force with a certain factor of safety. If the clamp design is minimised such that it can deliver the design specified clamping force at its peek performance, a small misalignment could reduce that performance below the minimum clamping force. This problem would not be noticed in a larger clamp design since it would be capable of producing more than

the specified clamping force. A reduction in the maximum force could still be in an acceptable range.

For ground based telescope systems, this problem would not be as significant since the slit mask could be removed from the instrument for periodic adjustments. However, orbital applications prohibit servicing the MARS and introduce large G-forces during launch. These G-forces could introduce misalignments between the clamp jaws which would not be noticed until the MARS is in service, long after possible repairs could be performed.

Chapter 7 Conclusions

7.1 Final Test Apparatus Design

The final configuration of the MARS clamp test apparatus is based on results of FEA models as well as experimental results. Initial FEA models of the MARS clamps showed that the optimum clamp design would deliver a maximum force of 1.33 N. The design of the test apparatus was focused around providing a maximum force measurement which exceeded this value with a comfortable margin.

The chosen method of providing a clamping force measurement is a test apparatus which employed the Lorentz Force to pull the clamp jaws open. This method required the design of a magnetic field generator as well as a current carrying coil. Producing a design for each was achieved by modeling potential designs using FEA models. Initially FEA was used to choose a method of producing a magnetic field. Permanent magnets were chosen due to their low cost, compact size and their ability to produce strong magnetic fields. Secondly, FEA was employed to optimise the design of the permanent magnet based field generator. The design of the flux return yolk was refined to improve performance and reduce complexity and cost.

The main design feature which dictated the maximum force deliverable by the apparatus was the force coil. The force coil is constructed from Copper wire wound around a magnetically inert core. The shape and size of the coil was chosen to produce the maximum number of turns in the wire while limiting the resistance of the coil to les than 500 Ω. The coil is powered by an available power supply which dictated the maximum resistance. The size of wire used for the coil was also examined. The end result is a force coil which, when powered to its maximum current could deliver 2.42 N of pulling force. Calibration produced a relation between driving current and force generated as well as the effects of misalignment.

Other components included a complex mounting system which secured the field generator assembly to the cryostat inner wall. This mount was capable of adjustments in six degrees of freedom which allowed for the precise alignment between the force coil and test clamp. A releasable clamp was also designed which allowed the link between the force coil and clamp jaw to float free for a period of time. This was included in order to allow the various components to contract during cool down without affecting the alignment between the force coil and the field generator. Other minor components such as the force link, the force coil support and the clamp jaw support assembly were optimised during testing.

7.2 Clamp Design Analysis

A single prototype clamp was tested for holding force using the test apparatus as well as a mass based procedure. It was found that it generally performed as expected based on simulations. An increase in clamping force was noticed with an increase in clamp coil current and at least on experiment was able to push the prototype clamp to saturation. Beside these simple characteristics, the clamp could not be made to perform in a repeatable manner. However, the FEA models presented represent a rough estimate of the clamp's potential and it was not unexpected that the results would not match with experimental results.

7.3 Recommendations

Experimental result showed that the test apparatus is a viable instrument for applying known forces to the clamp jaws. Its use is not limited to the MARS experiments but could be expanded to include any experiment which requires the application of high accuracy forces in an enclosed cryogenic environment.

Although a test apparatus is developed to characterise clamp geometry, material, response at temperatures neat 30 K in a high vacuum, the clamps themselves limited the original scope of the research. This stemmed from the inability to accurately and consistently align the two halves of the clamp assembly. If the clamp jaws could be properly aligned, the repeatability of the experiments would be improved. It is recommended that the test apparatus be employed in further experiments which also include a greater degree of confidence in the alignment of the MARS clamp jaws.

The MARS clamps themselves require a design re-evaluation. Their susceptibility to misalignment makes them ill-suited to applications in orbit which would have to survive launch conditions as well as extended operation without service. It will be difficult to minimise the clamp design given the degree of variability in performance. A more dependable design should be developed.

References

[1] J.W. Cornelisse, "Technical Requirements Document for the Definition Study of the Near-Infrared Spectrograph for NGST", PF-NGST-TRD-101, issue 1, ESA/ESTEC, Noordwijk, 2001

[2] Darren A. Erickson, "Design of a Mechanically Actuated Reconfigurable Slit mask (MARS) for the NGST near IR Spectrograph", National Research Council of Canada, Herzberg Institute of Astrophysics.

[3] Richard P Reed, Alan F. Clark, *Materials at Low Temperatures,* American Society for Metals, Menlo Park Oh, 1983

[4] *Alloy Data Sheets,* CRS Holdings, Carpenter Technology Corporation,

[5] Gordon B. Bowden, "Magnetic Forces Inside Permanent Magnet Assemblies" ABC Technical Note No. 067, 1992

[6] David Meeker, *FEMME User's Manual*, http://femme.berlios.de, 2002

[7] Comsol Ab. *FEMLAB 3, Electromagnetics Module User's Guide*, 2004

[8] N. Sato et al., *Force Measurement of a Superconducting-Film Actuator for a Cryogenic Interferometric Gravitational-Wave Detector,* 2003 Elsevier Science Ltd.

[9] B. Subramonian et al., *A New Ball-On-Disk Cryogenic Wear Test Rig,* 2005 Elsevier Science Ltd.

[10] Franz Keplinger et al, *Lorentz Force Based Magnetic Field Sensor with Optical Readout,* 2003 Elsevier Science Ltd.

Appendix A – Clamp Simulation Geometries

Experiment #	Description (Leg Dimensions are W x H)	Clamping Force [N/mm] Hymu 80	Clamping Force [N/mm] High-Perm 49
1	Original design	0.1693	0.1682
2	Original with rounded corners	0.1693	0.1686
3	2mm x 5mm legs and 2mm core	0.1139	0.1134
4	Notched corners	0.1158	0.1154
5	4mm x 6mm legs	0.2244	0.2235
6	Notched lower beam 0.5mm notch	0.1679	0.1672
7	Notched lower beam with filleted inner corners	0.168	0.1673
8	Original with 2.5mm x 12mm coil	0.1691	0.1684
9	#8 with 4mm x 5mm legs	0.225	0.224
10	#8 with 4mm x 4mm legs	0.2251	0.2242
11	semicircular core; r1=6mm, r2=9mm, equivalent coil areas	0.1695	0.1689
12	Flat coil core filleted legs; r1=4mm, r2=7mm	0.1695	0.1687
13	#10 with 5mm x 4mm legs	0.279	0.2779
14	#10 with 6mm x 4mm legs	0.3338	0.3329
15	#10 with 7mm x 4mm legs	0.3857	0.3874
16	#10 with 8mm x 4mm legs	0.3997	0.4421
17	#10 with 7.5mm x 4mm legs	0.4034	0.4146
18	#10 with 6.5mm x 4mm legs	0.3606	0.3602
19	7mm x 4mm legs with filleted ends and no mounting bar	0.3852	0.3863
20	#15 with rounded outer end	0.3859	0.3874
21	#17 with rounded outer end	0.4045	0.4146
22	#21 with modified mounting bar	0.4027	0.4149

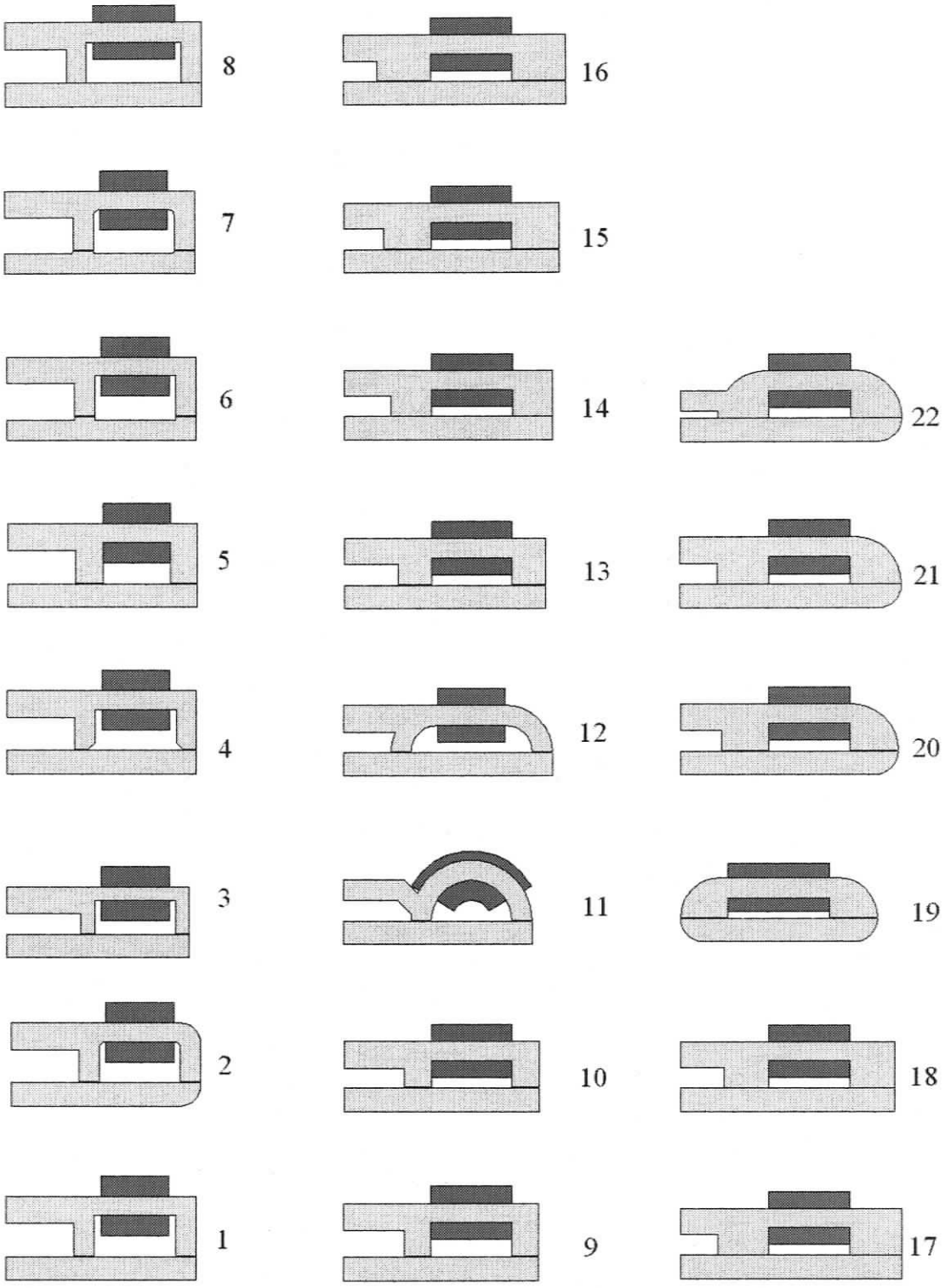
8
16
7
15
6
14
22
5
13
21
4
12
20
3
11
19
2
10
18
1
9
17

Appendix B - Helmholtz Coil Pair

Helmholtz coil pairs are another common method for generating a magnetic field. A Helmholtz coil pair consists of two parallel coils driven in phase and spaced one radius apart as shown in Figure B-0-1. The main advantage to a Helmholtz pair is the ability to generate a region of uniform magnetic field generated at its center. The size of this region is dependant on the diameter of the coils. Drawbacks include the volume of coil needed to generate a strong magnetic field and heat generated by the coils.

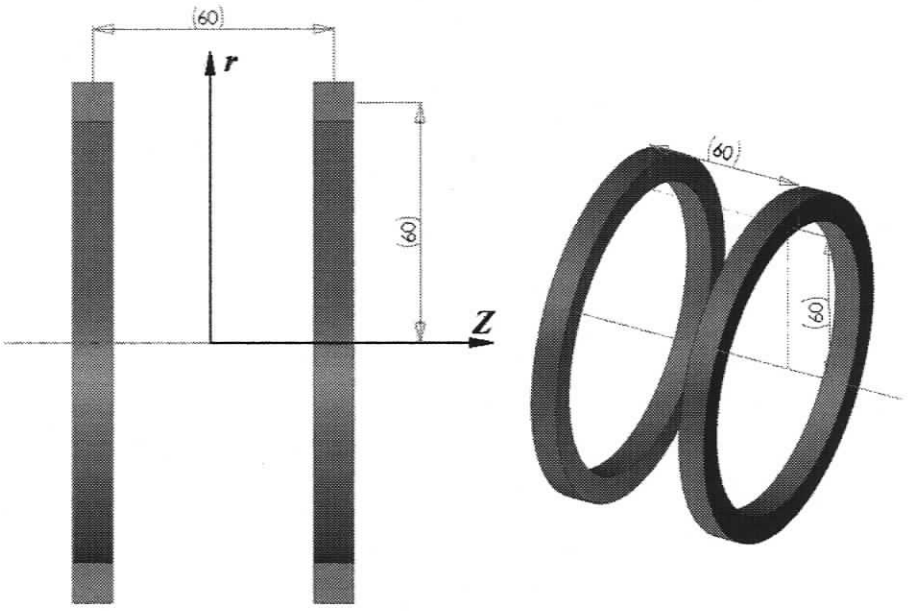

Figure B-0-1: Isometric and section view of a Helmholtz coil pair with a radius and spacing of 60mm

B.1 Magnetic Field Generated in a Helmholtz Coil

The strength of the magnetic field generated in a Helmholtz coil pair is proportional to both the number of turns of wire in the coils as well as the current in the wire. The strength of the field at r = Z = 0, can be roughly approximated by the relation shown in equation (8.1).

$$H = nI / L \tag{8.1}$$

Where H is the magnetic field strength, N is the number of turns, I is the wire current and L is the length of the coil. The flux density B which is shown in equation (2.3) can be expressed in the form shown in equation (8.2)

$$B = \mu_0 (H + M) \tag{8.2}$$

The value M is the magnetization, and is a property of the material inside the magnetic field. Since the Helmholtz coil will be in a vacuum and will not have a magnetic core, the magnetization can be ignored and equation (8.2) simplifies to equation (8.3).

$$B = \mu_0 H \tag{8.3}$$

The flux density is an important quantity when the Lorentz Force calculations are performed on the FEA results.

B.2 Coil Windings

The physical characteristics of the Helmholtz coils are important to the simulation process. The number of turns and the wire current are both integral to defining the strength of the magnetic field inside the coil pair. This information will also be used while determining size and shape of the force coil. In order to clarify the discussion of the coil windings the following nomenclature must be introduced.

- I_w = wire current
- I_{hhc} = Helmholtz total coil current
- J_c = current density in the coil
- A_{coil} = cross-sectional area of the coil

The wire current is the current supplied by the power supply to the coil. The coil current is simply the sum of the currents from all the windings in the coil and is given by equation (8.4).

$$I_{hhc} = nI_w \tag{8.4}$$

The current density is the current per unit cross-sectional area of coil and given by equation (8.5). The units of current density are A/m^2.

$$J_c = \frac{I_{hhc}}{A_{coil}} \tag{8.5}$$

The size of wire used to wind the coils is also examined. Finer gage wire allows for more windings in a given cross-sectional area while heavier can handle higher current. These properties lead to a trade off between n and I in equation (8.4).

The current carrying capacity of a conductor can be expressed as a function of its cross-sectional area. The current handling values given in Table B-1 are derived using a standard value for copper wire. The value chosen is 750 circular mils/A. This converts to 0.380 mm^2/A and is divided into each wire's circular area to yield the current capacity. Copper wire was chosen because of its high conductivity, availability, and low cost.

Table B-1: Properties of standard copper wire [IEEE Standard 835]

AWG	Diameter, d [mm]	Circular area A_c [mm^2]	DC Resistance [Ohms/m]	Max Current [A]
36	0.127	0.01267	1.4600	0.03333
34	0.16	0.02011	0.9186	0.05290
32	0.203	0.03237	0.5709	0.08517
30	0.254	0.05067	0.3707	0.13333
28	0.33	0.08553	0.2129	0.22506
26	0.409	0.13138	0.1430	0.34572
24	0.511	0.20508	0.08957	0.53965
22	0.643	0.32472	0.05512	0.85446

The number of turns of a particular sized wire that can be fit into a coil cross-section of A_{coil} can be approximated by dividing A_{coil} by the square of the diameter of the wire as shown by the first relation in equation (8.6). This approximation assumes that the windings of the coil are perfectly laid. Although this isn't a perfect representation, it is very close to reality and will suffice for the purposes of this analysis. Coil sizes of ten different cross-sections are considered. The coils ranged in area from 1 cm^2 to 30.25cm^2 and the number of turns for each coil is calculated for all wire gages outlined in Table B-1. The number of turns ranged from 242 turns for 22AWG wire in a 1cm^2 coil to 187550 turns for 36AWG wire in a 30.25cm^2 coil.

Since the current carrying capacity and the number of turns in a given cross-section are both directly related to the cross-sectional area of the wire, the total coil current I_c is the same regardless of the gage of wire used for winding. This property is shown below.

$$\begin{aligned} n &= \frac{A_{coil}}{d^2} \\ I_w &= \frac{1}{k}\left(\frac{1}{4}\pi d^2\right) \\ I_c &= nI_w = \frac{A_{coil}}{d^2} \times \frac{1}{k}\left(\frac{1}{4}\pi d^2\right) = \frac{1}{4k}\pi A_{coil} \end{aligned} \tag{8.6}$$

Equation (8.6) derives an equation for the total current in a coil of given area A_{coil}. The term *"k"* is the constant 0.380mm^2/A discussed above. It can be seen that the total current is independent of the wire diameter d and therefore the total current I_c in a coil is dependent only on the cross-sectional area of the coil. Since J_c is given by equation (8.5), it can be seen that A_{coil} drops out and the current density for all coil sizes and all wire gages is constant. This constant is derived in equation (8.7) and indicates the maximum current density at which the Helmholtz coils can be driven. This is an useful quantity as the FEA software required current density as input for calculating magnetic fields and forces.

$$J_c = \frac{I_c}{A_{coil}} = \frac{\frac{1}{4k} A_{coil}\pi}{A_{coil}} = \frac{1}{4k}\pi = \frac{\pi}{4\left(.380\times10^{-6}\ m^2/A\right)} = 2.0668\,MA/m^2 \qquad (8.7)$$

B.3 Heat Generation in the Coils

The heat generated by the current flowing through the coil is given by the same power relation shown earlier in equation (2.1). I_w is known but the resistance R of the coil is dependent on the length of the wire in the coil which is in turn dependent on the wire gage, the coil cross-sectional area and the radius of the coil.

The length of the wire needed to wind a coil can be approximated by first calculating the volume of the windings and then dividing by the wire diameter squared (d^2). This method is similar to the method which was used to find the number of turns in each coil and is not perfect but sufficient. The wire length, resistance and heat generation is calculated for coils of various cross-sectional areas and central radii. It was found that the power generated by the coils is independent of the wire gage. This is similar to the findings outlined above for the total coil current I_c.

The heat generated depends on both the coil cross-sectional area and its radius. Therefore a large number of combinations are considered. The highest heat generation is 11.47 W and is found in the largest coil simulated. This coil had a 5.5 cm x 5.5 cm cross-section and a central radius of 6cm. This value is the heat generated by only one of the coils in the pair. Therefore, the heat generated by the complete field generator of this size would be 22.96 W.

B.4 FEA Field Strength Simulations

The magnetic field inside the coil is modeled for ten coil cross-sections and four coil radiuses. In some cases, it is impossible to calculate a specific coil configuration due to geometry restrictions. For each model, the current density is set at the theoretical maximum shown in equation (8.7). The coil cross-section and radius is systematically altered to yield the results shown in Table B-2. The values shown are the magnitudes of B

in the region of constant *B* near the center of the coil. It can be seen that the field inside the coil is quite low. The largest coil only yielded a flux density of 0.0493T. Blank entries indicate coil configurations which are geometrically impossible to create.

Table B-2: Magnitude of the magnetic flux density at center of the Helmholtz coil pair

Coil Radius [cm]	Max Magnetic Flux at center [T]									
	1cm x 1cm	1.5cm x 1.5cm	2cm x 2cm	2.5cm x 2.5cm	3cm x 3cm	3.5cm x 3.5cm	4cm x 4cm	4.5cm x 4.5cm	5cm x 5cm	5.5cm x 5.5cm
3	0.00306	0.00703	0.0125	0.0197	-	-	-	-	-	-
4	0.00233	0.00522	0.00933	0.0146	0.0212	0.0291	-	-	-	-
5	0.00186	0.00419	0.00749	0.0117	0.0169	0.023	0.0304	0.0386	-	-
6	0.00156	0.00353	0.00623	0.00979	0.0141	0.0192	0.0252	0.0321	0.0399	0.0493

It can already be seen that the flux density generated by the Helmholtz coil pair does not compare well with that of the permanent magnet based field generator. In fact, the largest, most powerful coil generates a flux density which is weaker than the weakest permanent magnet configuration. In the interest of completeness, force simulations are performed on the Helmholtz coil pair.

B.5 Force Simulations

The largest Helmholtz coil pair is simulated using the same application mode that is used for the permanent magnet force simulations. The force calculated is 2.34N using a $1cm^2$ force coil. This force is slightly more than half that which was found for the 0.0254 m deep permanent magnet based field generator and only 13.4% the strength of the best permanent magnet. It is also worthy to note that this Helmholtz coil is extremely large. Its outer diameter is 17.5cm and there is a mere 0.5cm gap between the coils in which the force coil must pass. Because of the poor performance observed from the best case Helmholtz coil pair, it is unnecessary to simulate the other Helmholtz configurations.